University of Glasgow
DEPARTMENT OF
AEROSPACE
ENGINEERING

VALIDATION OF THE NEW VERSION PNS3DT CODE

H.-L. ZHANG and B. E. RICHARDS

G. U. Aero Report No. 9401

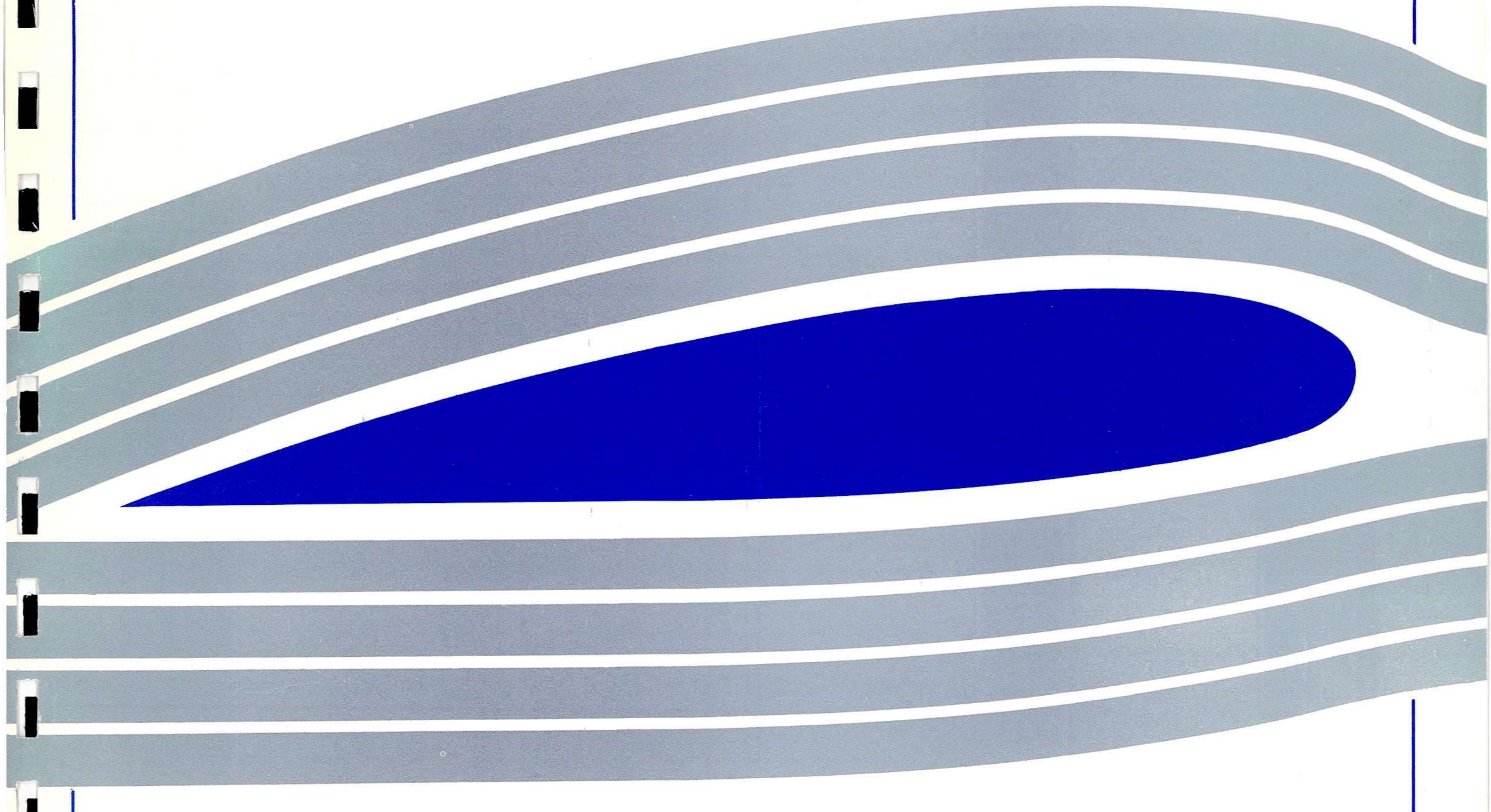

VALIDATION OF THE NEW VERSION PNS3DT CODE

H.-L. ZHANG and B. E. RICHARDS

G. U. Aero Report No. 9401

Department of Aerospace Engineering
University of Glasgow
Glasgow G12 8QQ

January, 1994

VALIDATION OF
THE NEW VERSION PNS3DT CODE

H.-L. ZHANG and B. E. RICHARDS

January, 1994

Abstract

In this study, the PNS3DT code developed in the University of Glasgow to solve steady compressible parabolized Navier–Stokes equations with Baldwin–Lomax turbulence model is updated. The choice of primitive variables in the numerical scheme, different wall temperature conditions as well as the effect of different grid stretching strategies are tested in detail. Excellent agreement between the numerical and experimental results is observed. Thus, the code could provide a powerful tool to predict the aerodynamics characteristics on the ogive cylinder surface and to simulate the complicate flow structures around the cylinder.

1. Basic Theory

The governing equations of steady supersonic or hypersonic viscous flow are the Navier–Stokes equations, which can be simplified for some simple cases by omitting the viscous derivatives in the streamwise direction (the so-called PNS: parabolized Navier–Stokes Equation). Its applications include the flow over ogive configurations, cone–cylinder combinations, and so forth. The equations can be numerically solved section by section marching in a streamwise direction.

The procedure is such that no outflow boundary conditions are necessary. In the first section and on the outer boundaries the uniform flow is forced in the calculation procedure, provided the shock waves are attached to the configuration and located in the domain of computational grids. Non–slip and zero normal gradient boundary conditions are used for velocity and pressure on the body surface, respectively. Either adiabatic wall or constant temperature wall conditions can be specified.

For turbulent flow, the Baldwin–Lomax[2] turbulence model is used to replace the molecular viscosity with turbulent viscosity. The Degani and Schiff's modification[4] to the Baldwin–Lomax turbulence model is also applied, when cross–flow separation appeared in the flow field.

2. The PNS3DT Code

In the PNS3DT code developed in the University of Glasgow[5, 7] the finite volume method is used to discretisize the Navier–Stokes equations, because of its conservative property.

Osher's approximate Riemann solver[6] is applied when calculating the fluxes at the cell boundaries, with which both shock waves and shear layers could be captured in fewer grid cells. In order to give a high order of accuracy, as well as to avoid oscillations at points of discontinuity, Van Leer's MUSCL scheme[1] is used in the code. All viscous terms in the Navier–Stokes equations are evaluated by proper interpolation of the variables in a way equivalent to the central difference scheme.

Since a time–dependent approach is applied to explicitly update all variables, the CFL number required is less than one.

The grid is generated by an algebraic grid generator using transfinite interpolation techniques. The grid is stretched close the wall and should be orthogonal at the wall.

3. Some Features of the New Version of the PNS3DT Code

1) Choice of primitive variables

In the new version of PNS3DT code, the pressure P is chosen as a primitive variable rather than the temperature T, because fewer iterations are required in the solution procedure. More importantly, less numerical dissipation is found when using P as a primitive variable, as shown in the comparison in Fig.1 for the Stanton number distributions of test case 3 (for the details of different test cases, see Table I). The iso–Stanton number lines are normal to the base of the ogive cylinder for P as variable, but not for T as variable, which means the level of numerical dissipation is different.

2) Constant temperature wall or adiabatic wall

If the wall temperature T_w is as inputted (not zero), then the code treats the wall as a constant temperature one. Otherwise, T_w is set to zero, which signals an adiabatic wall in the code. There is little influence observed to the C_p distribution on the wall either from the adiabatic or from the constant temperature boundary conditions, see Fig.2.

3) Grid effect

Grid distribution is found to have a great influence on the numerical results. We have tested different grid distribution strategies as well as different numbers of grid cell.

The grid is generated using a transfinite interpolation method (algebraic grid generation). Given $IN\text{x}KN$ points on the body surface, $IN\text{x}KN$ straight lines normal to the surface at corresponding points with length of R could be generated, and divided into JN intervals, thus giving $IN\text{x}JN\text{x}KN$ grid cell corners.

However, there are two grid interpolation strategies. Let us take the grid in the leeside symmetric plane as an example. The distances at the leading edge and trailing edge are denoted as RLU and RTU. Because RLU is very small while RTU very large, and that at least several grid points should be located in the boundary layer for Navier–Stokes calculation, we should take different stretching parameters at the leading edge section and trailing edge sections, respectively. The problem is how to obtain the grid distributions between these two sections.

Grid A

The stretching parameters in the stretching functions are interpolated linearly according to the distance away from the leading edge. Thus the grids between the leading and trailing edge sections are generated using different stretching parameters. So, this grid is called the parameters interpolation grid.

Grid B

Given the distributions of R at leading and trailing edge sections, the other R between them could be generated by direct linear interpolation. Thus, this grid is called coordinates interpolation grid.

Fig.3 shows the grids obtained using these different interpolation strategies, and a smoother grid distribution for *Grid B* than for *Grid A* is observed. The grid distribution has also influence to the convergent history. In Fig.4 is shown the iterative numbers necessary for convergent results at each

section for two interpolation strategies: the curve for *Grid A* has serious oscillations in the marching procedure.

The final numerical results are also different for *Grid A* and *Grid B*. Fig.5 shows the comparison of Stanton number distributions on the surface. Because the Stanton number is determined by the gradient of temperature normal to the body surface, its distribution is determined by the normal distance between the first grid line and the body surface. Therefore, the grid should be carefully calibrated to give the correct results.

Fig.6 gives the comparison between the coarse, moderate and fine grids. It is obviously that the physical phenomena could not be captured if the grid is too coarse like that shown in Fig.6a. Only primary separation is observed, while secondary separation is shown for the other two grid calculations.

4. Numerical Results and Comparison with Experiments

Table I shows the incoming flow condition for the test cases in this study. The experiments are carried out at DRA Bedford[3]. For Cases 1 and 2, the outer boundaries of the numerical grid should be extended far enough to include all flow features such as shock waves. If not, the shock wave will be reflected from the outer boundaries with the result that the iterative procedure fails to be convergent.

Case No.	M_∞	AoA	Re	$T_o(K)$
1	1.45	14	2x10^6/ft	301
2	1.80	14	2x10^6/ft	304
3	2.50	14	4x10^6/ft	308
4	3.50	8	4x10^6/ft	315
5	3.50	14	4x10^6/ft	315

Table I

1) Surface properties

a) C_p distributions:

In Figs.7–11 are shown the C_p distributions on the body surface for Cases 1–5 and the comparison between the computational and experimental results. The agreements between them are generally good. It seems that the numerical results at low M_∞ agree better with the experimental results than at high M_∞. Thus, the comparison for Case 5 seems the worst. In addition, the details in the separation region could be resolved in numerical results, and stronger gradients in C_p distributions are observed in these regions than that in experimental results.

b) Other surface characteristics

One of the most interesting characteristics of interest to industry concerns the shear stress distribution on the surface, because lift and drag forces on the body could be integrated from them. Fig.12 shows the numerical shear stress distribution for Case 3. It can be seen that the shear stresses reduce to zero on the separation and reattachment lines.

In Fig.13 is shown the limiting streamlines on the surface, plotted based on the shear stress distributions. The primary separation and reattachment lines are very obvious, while the secondary separation and reattachment lines can also be identified. The flow phenomena is very complicated in this separation region. The next subsection provides details of the analysis.

For the adiabatic wall, the Stanton number will be zero. However, the temperature should change on the wall due to the convective and diffusive effects in the flow procedure. Fig.14 shows the temperature distribution on the surface, where near the separation and reattachment lines the temperature is much higher than that in other places, mainly because of the strong convection behaviour appearing there.

2) Cross section flow

Numerical analysis from the computation results could provide more details in the flow field than that in the experiments, if the numerical mesh is fine enough, which signals limitations in experimental techniques.

a) Pitot pressure

The Pitot pressure distributions for Cases 1–5 are plotted in Fig.15–19 for three sections at $x=5.5D, 8.5D, 11.5D$, respectively, and compared with the corresponding experimental results shown in the right–hand side in these figures. The agreement is excellent, except for section 2 in Case 1, which presently cannot be explained.

The positions of the primary vortex vary with the angle of attack of the ogive cylinder and with the Mach number of the incoming flow. Usually there appears a secondary vortex, and for some cases (Case 3, for example) an even smaller vortex could be induced. In the experiments, it is very difficult to do measurements in the vicinity of the wall, and thus the Pitot pressure is available only at a distance away from the wall in these plots.

b) Other cross section flow characteristics

As mentioned before, the numerical simulation could provide a powerful tool to analyse the details of the flow field. In Fig.20 is shown the velocity vector for Case 3 at section $x=11.5D$. The flow topological structure could be seen more clearly if the particle lines in the flow field are plotted, see Fig.21. The separation points D and attachment points A are distributed alternately on the body surface. Besides the front and rear stagnation points, three separation points and two attachment points can be found. In the space above the body, three saddle points S and five spiral points V can be observed. The number of all these points should satisfy with the topological laws.

In addition, in Fig.22 is shown the vorticity contour for the same section which confirms the analysis based on the particle lines.

As to the space structure of the flow field, Fig.23 shows the C_p distributions in the symmetric windwardside, leeside, body surface and two section planes. The shock waves around the cylinder as well as the expansion waves on the shoulder of the ogive cylinder can be clearly identified. The wave development in the complicated vortices interaction region in the leeside of the cylinder can also be observed.

5. Conclusions

Based on the numerical tests completed in this study, it is concluded that the PNS3DT code developed in the University of Glasgow could provide a powerful tool to predict the aerodynamics characteristics on the ogive cylinder surface and to simulate the complicate flow structures around the cylinder. Excellent agreement between the numerical and experimental results is observed, while the computational analysis of the flow structure in the vicinity of the body surface could be an indispensable supplement to the experiments.

6. Acknowledgement

This research was sponsored by the DRA, Bedford with T.J.Birch as technical monitor. We are also grateful to Dr. X.Xu for his helpful suggestions in the course of the study.

References

[1] Anderson, W.K., Thomas, J.L. and Van Leer, B. (1986): A comparison of finite volume flux vector splitting for the Euler equations, *AIAA J., Vol.24, pp.1453–60*

[2] Baldwin, B. and Lomax, H. (1978): Thin approximation and algebraic model for separated turbulent flows, *AIAA Paper 78–257*

[3] Birch, T.J. (1993): Private communication.

[4] Degani, D. and Schiff, B. (1986): Computation of turbulent supersonic flows around pointed bodies having cross–flow separation, *J. Comp. Phys., Vol.66, No.1, pp.173–196*

[5] Jin, X.–S. (1993): A 3–d parabolized Navier–Stokes equations solver with Baldwin–Lomax turbulence model, *University of Glasgow, Aero Report 9315, July, 1993*

[6] Osher, S. and Solomon, F. (1982): Upwind difference schemes for hyperbolic systems of conservation laws, *Math. Comp., Vol.38, pp.357–372*

[7] Qin, N. (1989): User's guide for NS3D code, *GU Report, April, 1991*

Appendix: Figures

Fig. 1

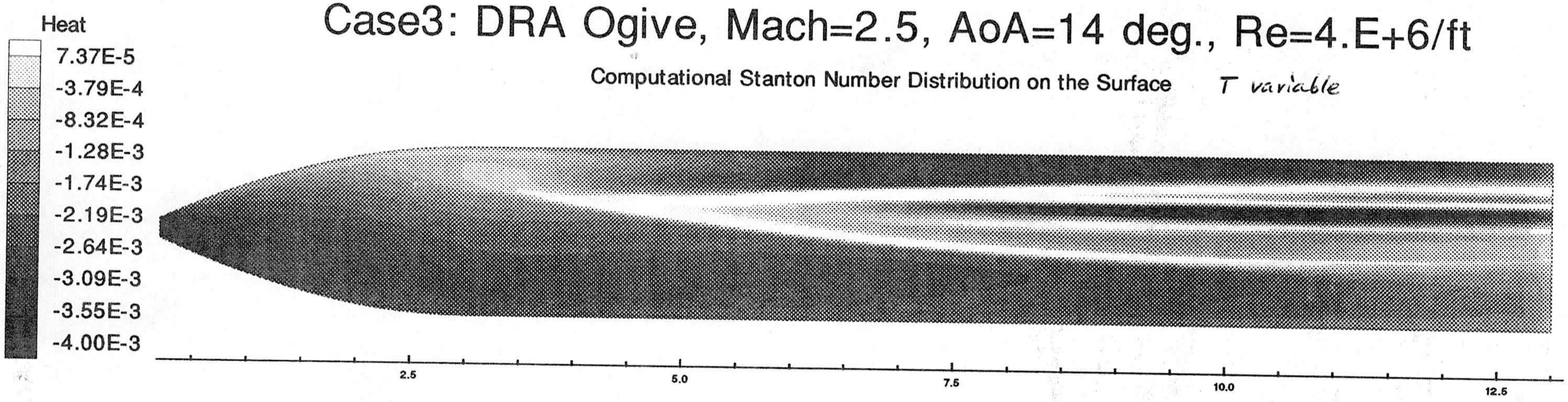
Case3: DRA Ogive, Mach=2.5, AoA=14 deg., Re=4.E+6/ft

Computational Stanton Number Distribution on the Surface T variable

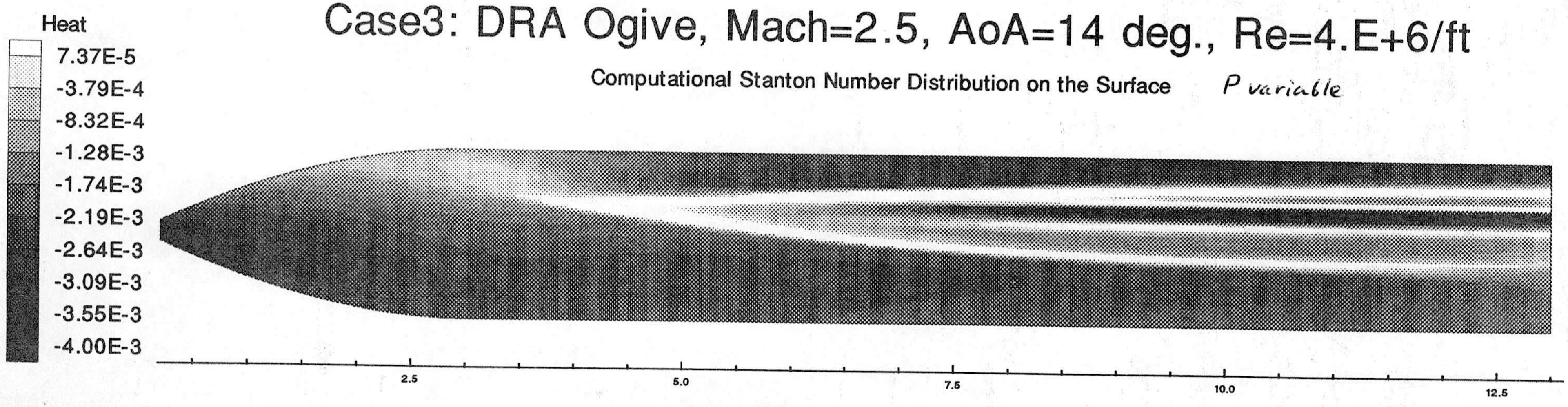
Case3: DRA Ogive, Mach=2.5, AoA=14 deg., Re=4.E+6/ft

Computational Stanton Number Distribution on the Surface P variable

Fig. 2

Case3: DRA Ogive, Mach=2.5, AoA=14 deg., Re=4.E+6/ft

Computational Stanton Number Distribution on the Surface: adiabatic wall

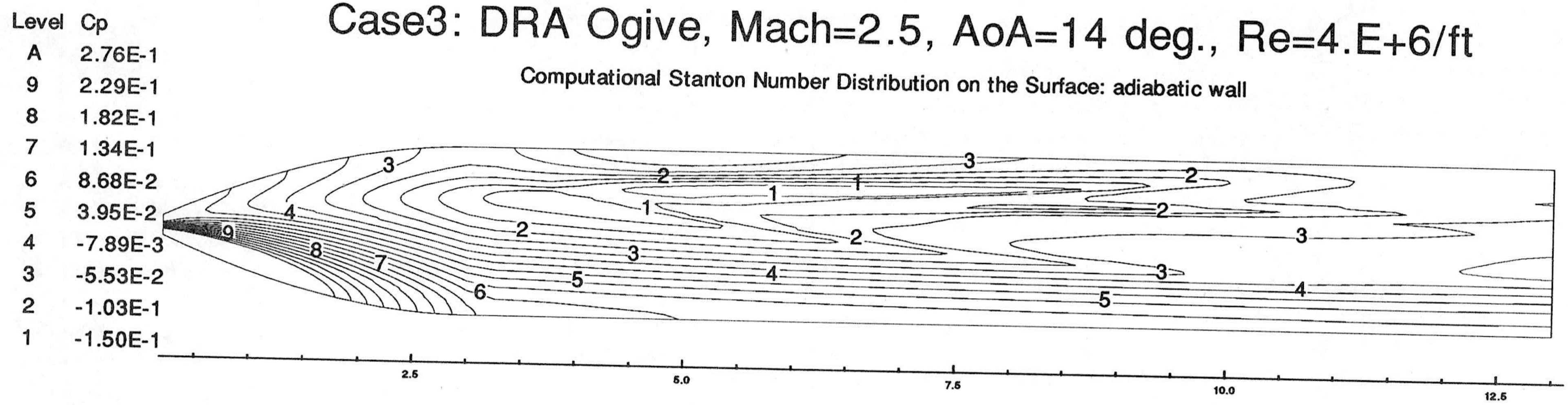

Case3: DRA Ogive, Mach=2.5, AoA=14 deg., Re=4.E+6/ft

Computational Stanton Number Distribution on the Surface: constant temperature wall

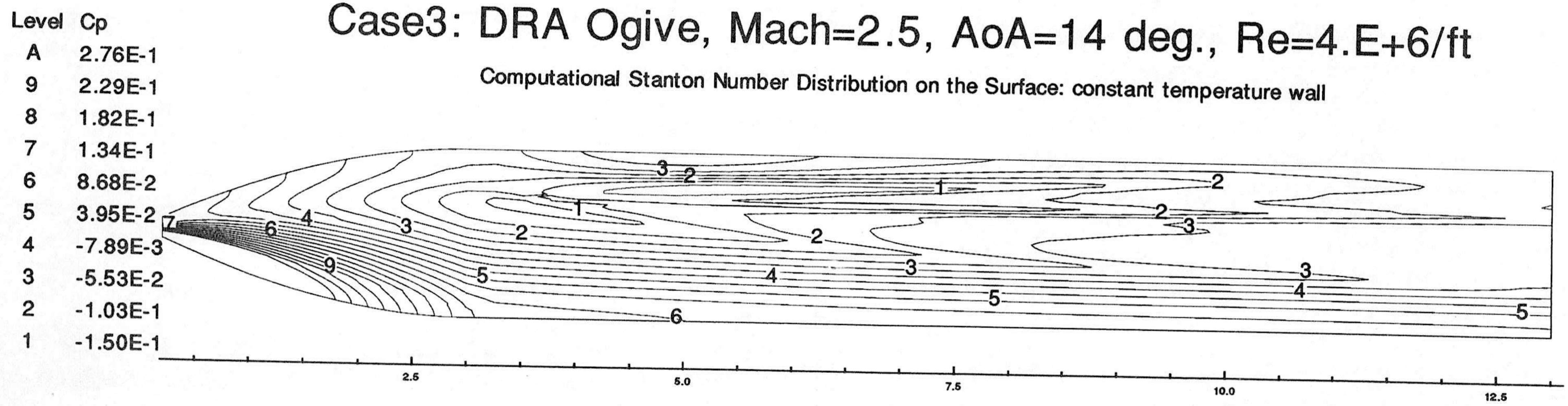

Fig.3

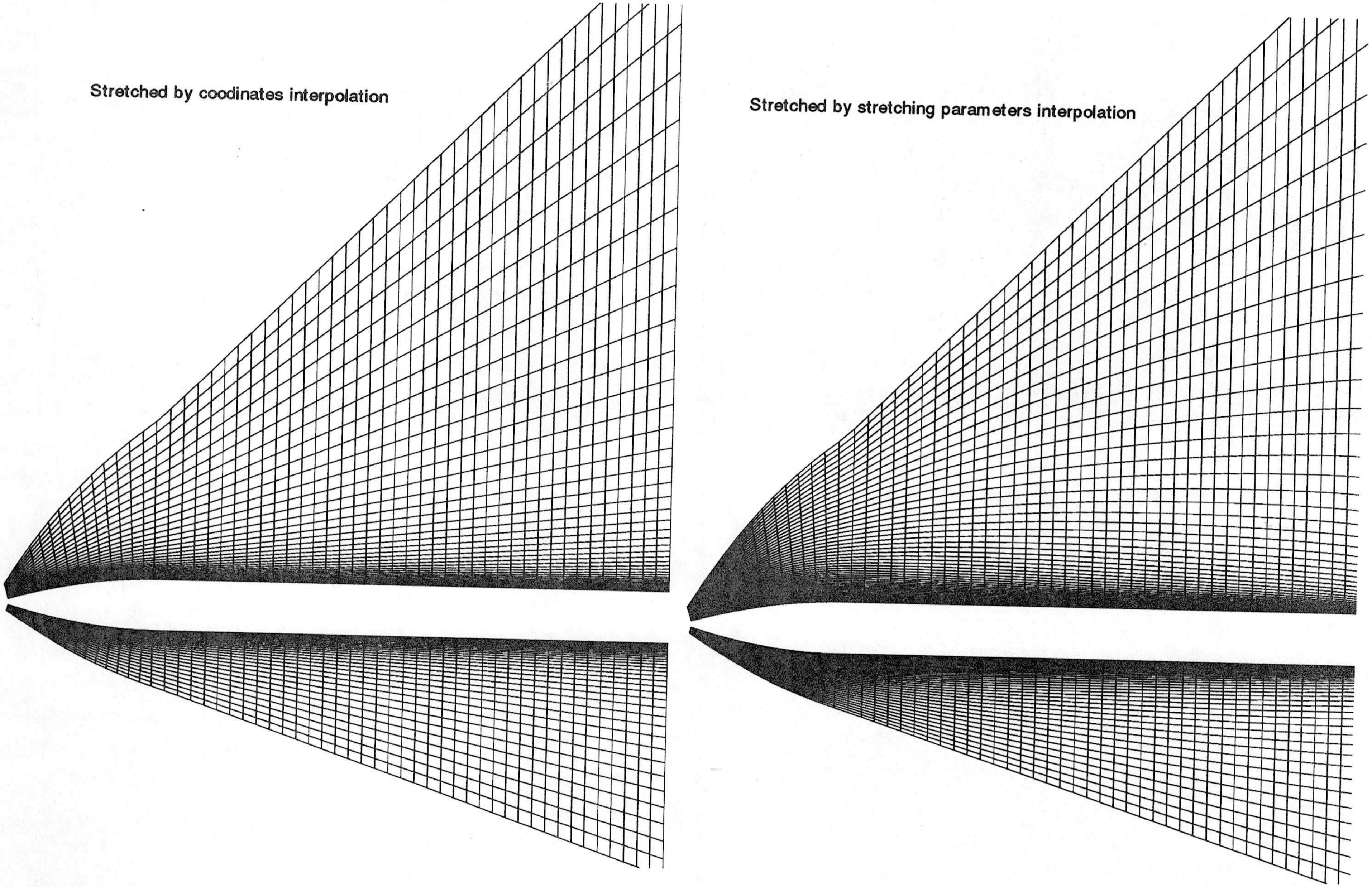

Stretched by coodinates interpolation

Stretched by stretching parameters interpolation

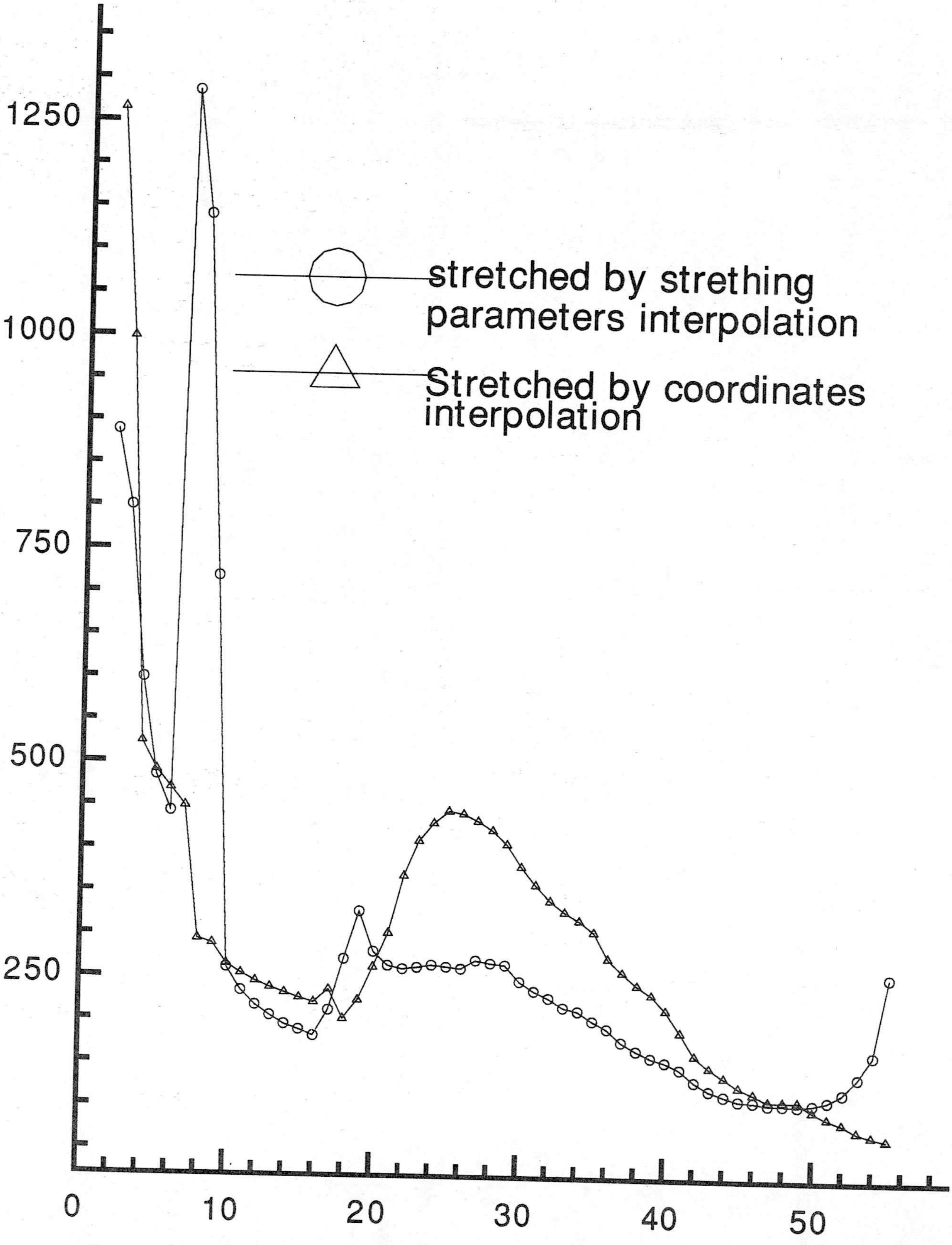
1250
1000
750
500
250
0
10
20
30
40
50
stretched by strething parameters interpolation
Stretched by coordinates interpolation

Fig. 4.

Fig. 5

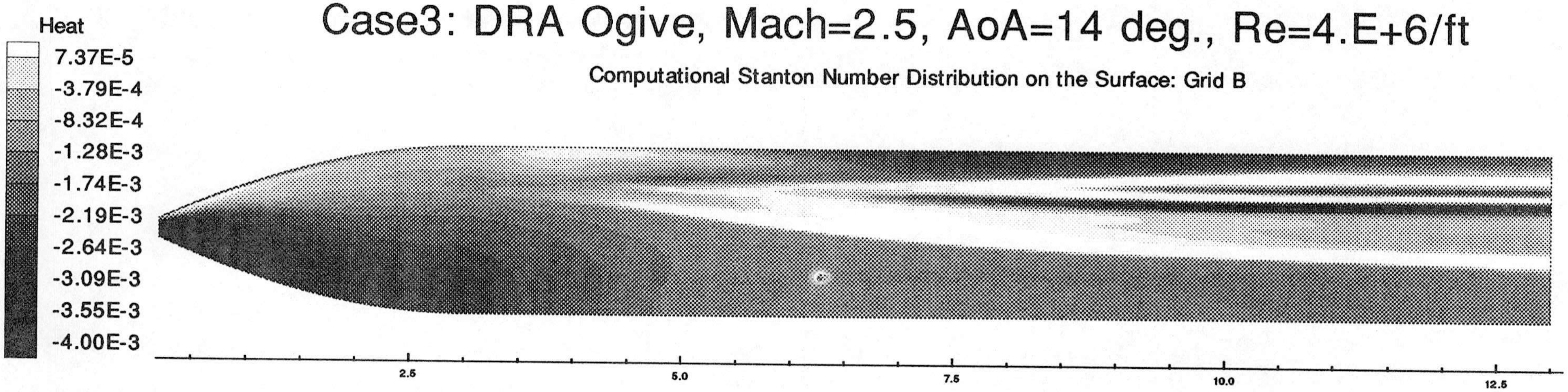

Case3: DRA Ogive, Mach=2.5, AoA=14 deg., Re=4.E+6/ft

Computational Stanton Number Distribution on the Surface: Grid B

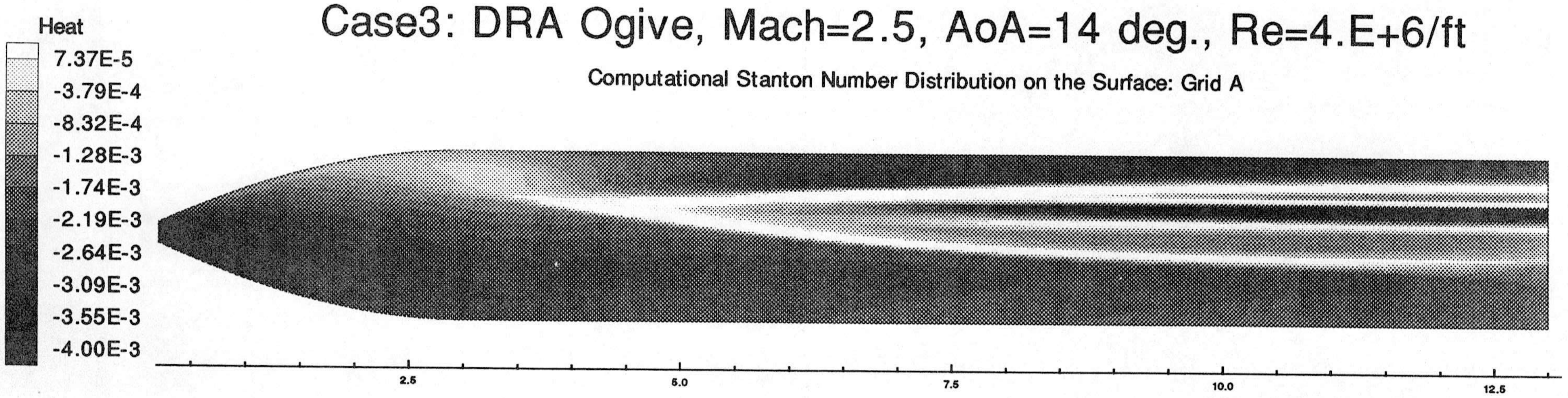

Case3: DRA Ogive, Mach=2.5, AoA=14 deg., Re=4.E+6/ft

Computational Stanton Number Distribution on the Surface: Grid A

Fig. 6

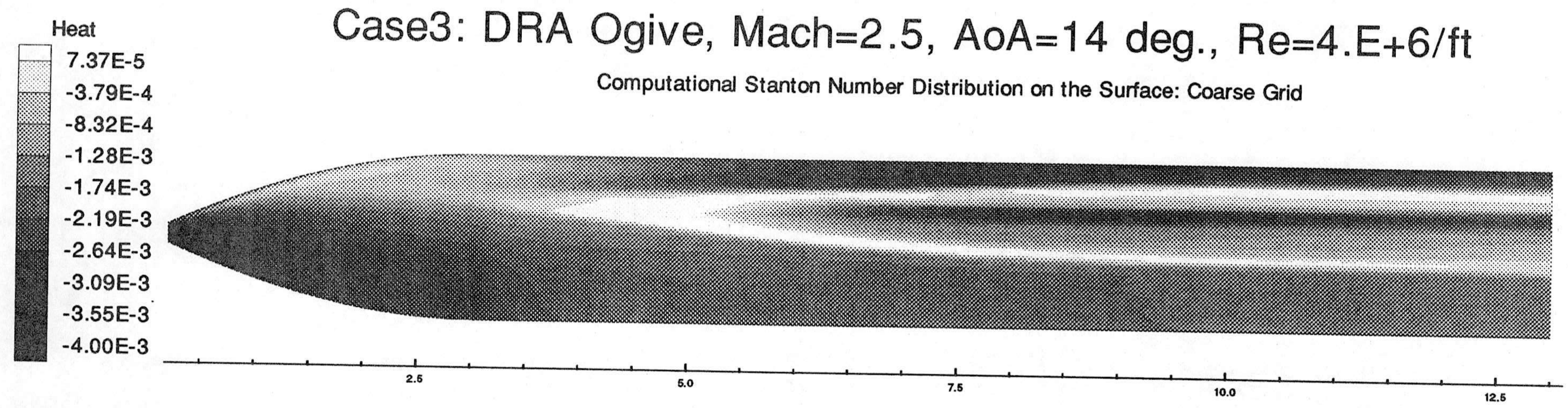
Case3: DRA Ogive, Mach=2.5, AoA=14 deg., Re=4.E+6/ft

Computational Stanton Number Distribution on the Surface: Coarse Grid

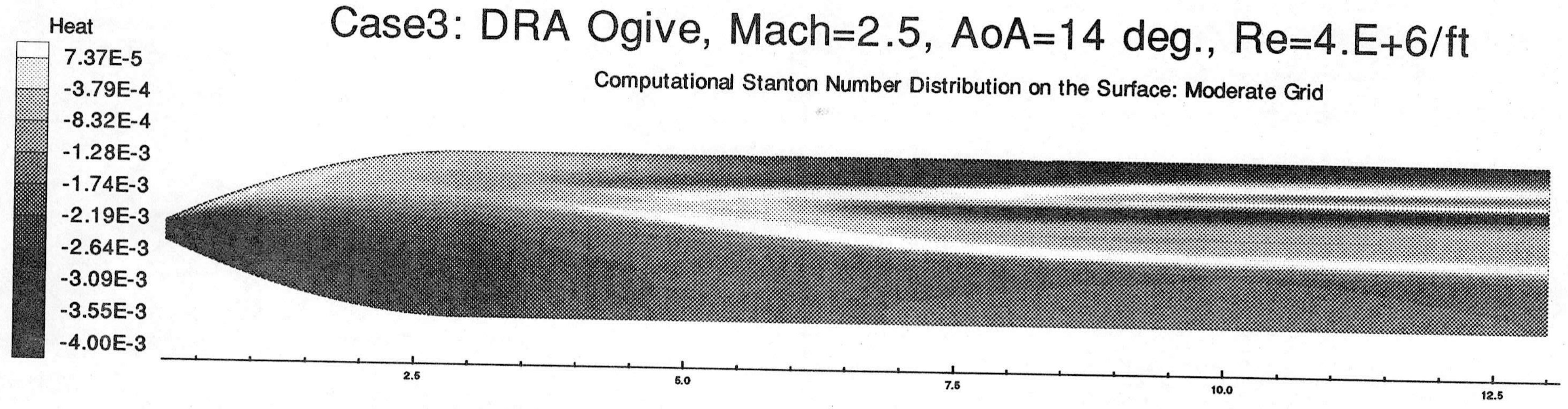
Case3: DRA Ogive, Mach=2.5, AoA=14 deg., Re=4.E+6/ft

Computational Stanton Number Distribution on the Surface: Moderate Grid

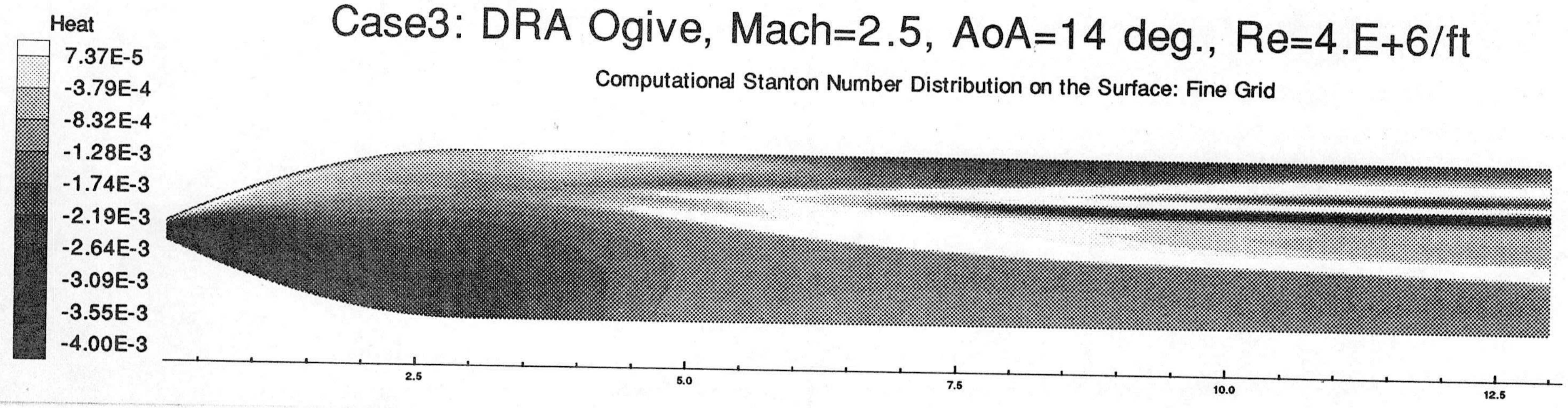
Case3: DRA Ogive, Mach=2.5, AoA=14 deg., Re=4.E+6/ft

Computational Stanton Number Distribution on the Surface: Fine Grid

Fig. 7

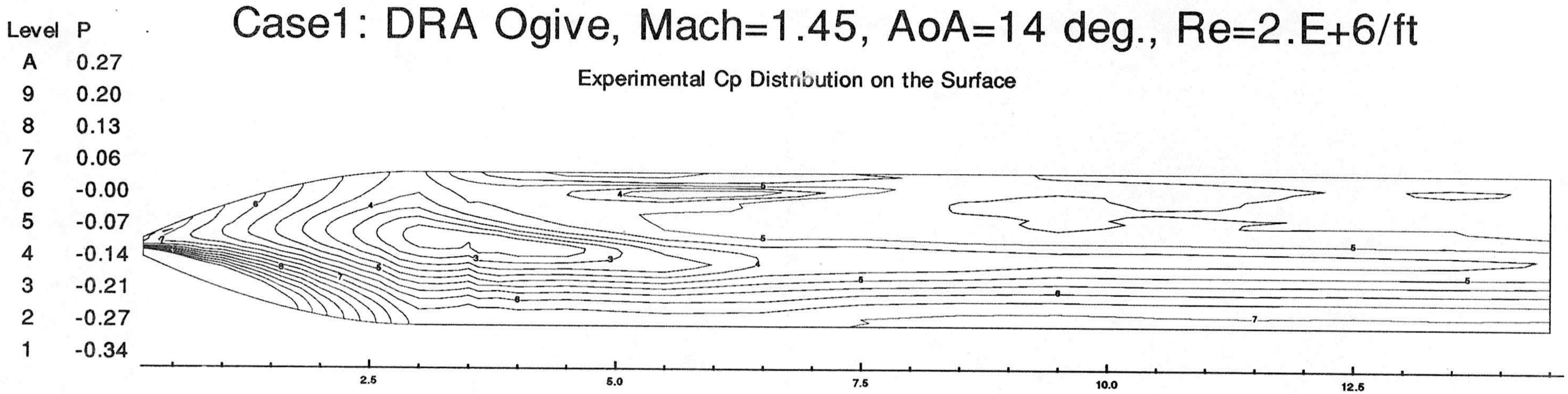
Case1: DRA Ogive, Mach=1.45, AoA=14 deg., Re=2.E+6/ft
Experimental Cp Distribution on the Surface
Level P
A 0.27
9 0.20
8 0.13
7 0.06
6 -0.00
5 -0.07
4 -0.14
3 -0.21
2 -0.27
1 -0.34
2.5
5.0
7.5
10.0
12.5

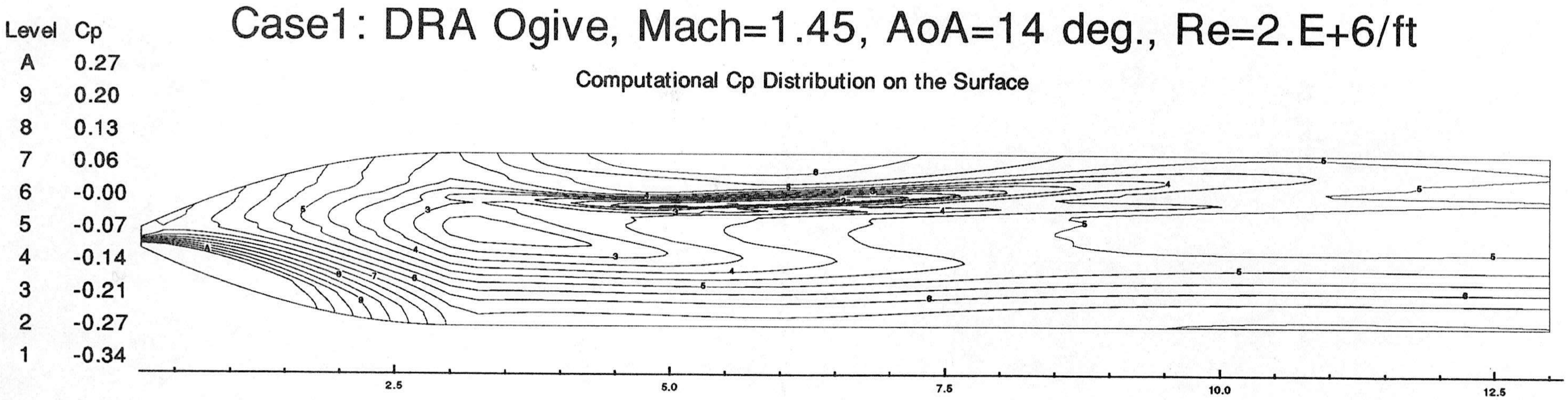
Case1: DRA Ogive, Mach=1.45, AoA=14 deg., Re=2.E+6/ft
Computational Cp Distribution on the Surface
Level Cp
A 0.27
9 0.20
8 0.13
7 0.06
6 -0.00
5 -0.07
4 -0.14
3 -0.21
2 -0.27
1 -0.34
2.5
5.0
7.5
10.0
12.5

Fig. 8.

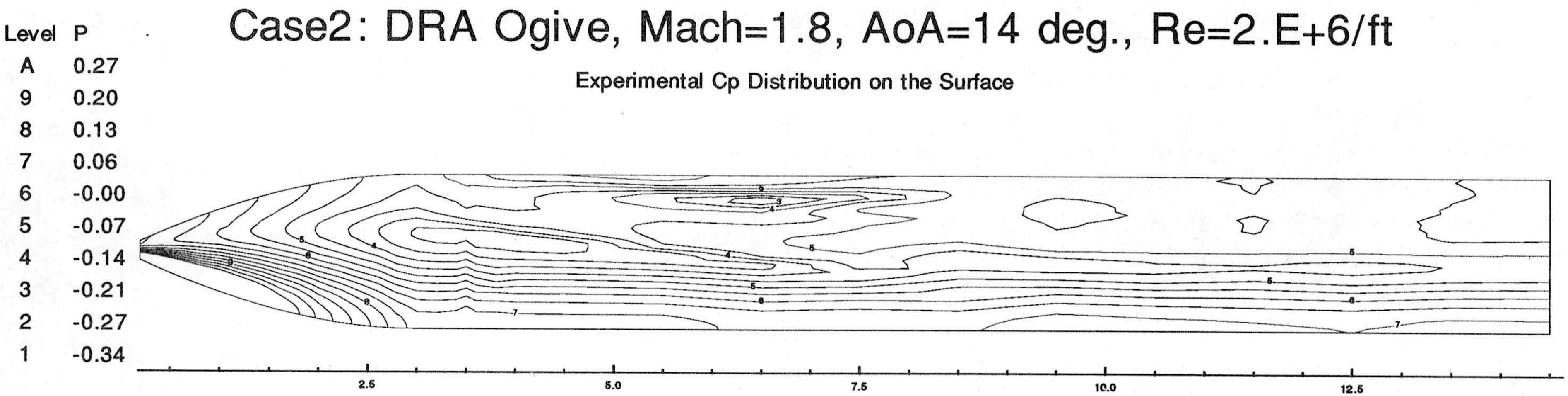

Case2: DRA Ogive, Mach=1.8, AoA=14 deg., Re=2.E+6/ft

Experimental Cp Distribution on the Surface

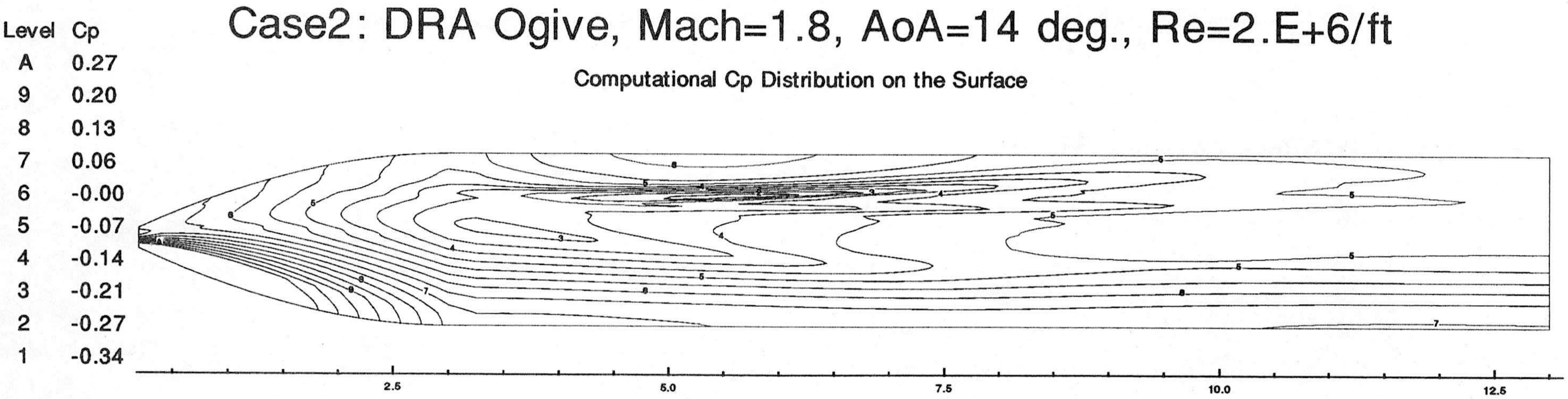

Case2: DRA Ogive, Mach=1.8, AoA=14 deg., Re=2.E+6/ft

Computational Cp Distribution on the Surface

Fig 9

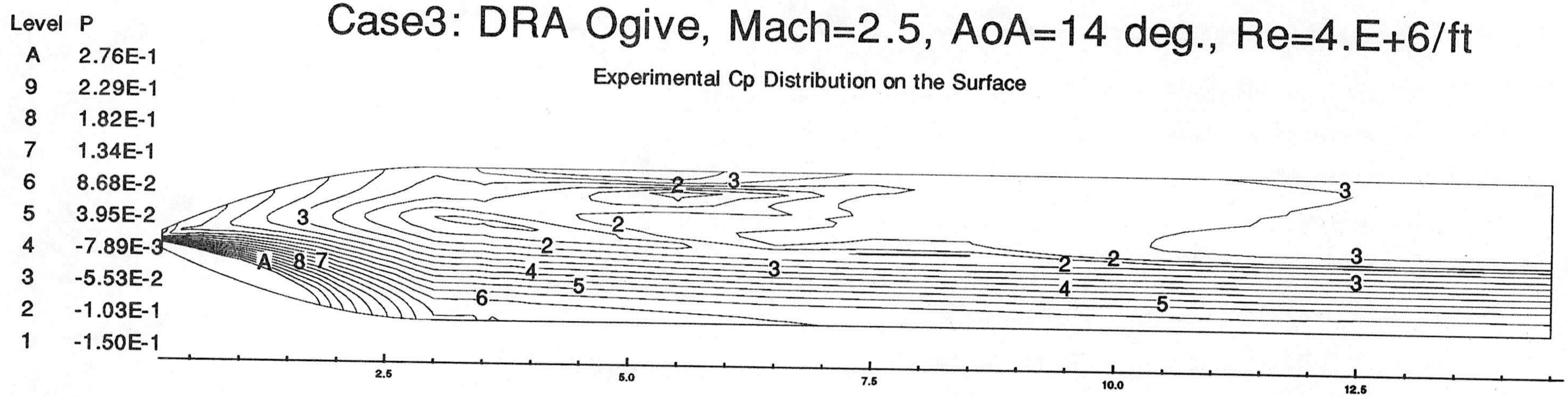
Case3: DRA Ogive, Mach=2.5, AoA=14 deg., Re=4.E+6/ft

Experimental Cp Distribution on the Surface

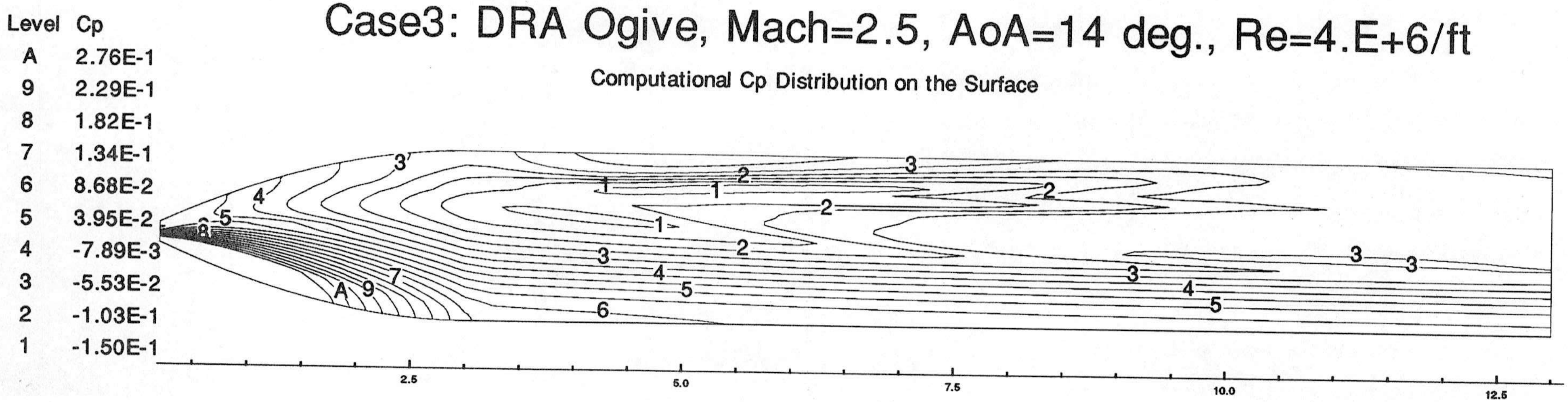
Case3: DRA Ogive, Mach=2.5, AoA=14 deg., Re=4.E+6/ft

Computational Cp Distribution on the Surface

Fig. 10

Case4: DRA Ogive, Mach=3.5, AoA=8 deg., Re=4.E+6/ft

Experimental Cp Distribution on the Surface

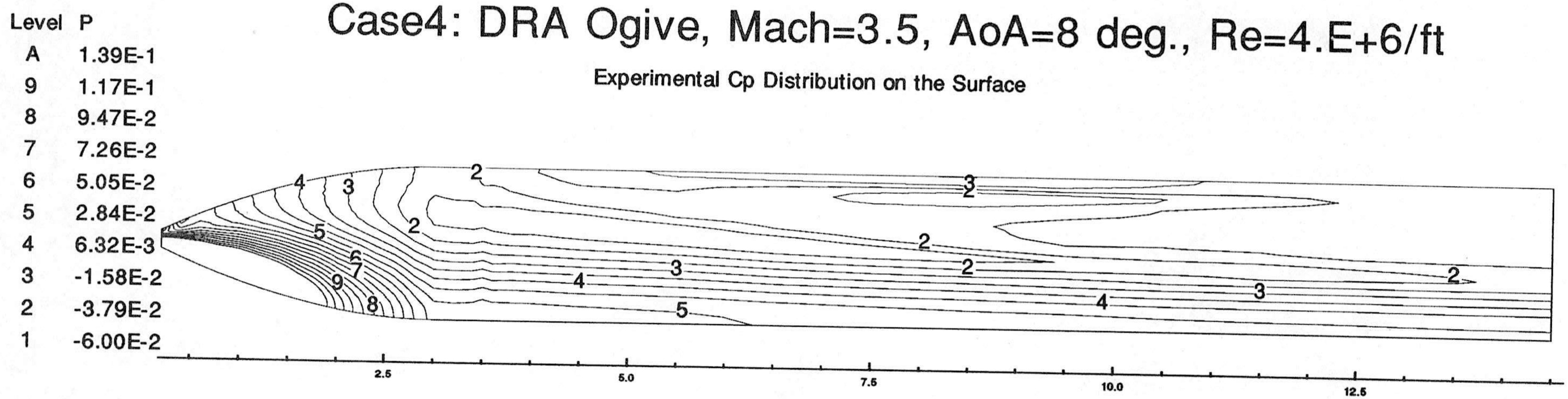

Case4: DRA Ogive, Mach=3.5, AoA=8 deg., Re=4.E+6/ft

Computational Cp Distribution on the Surface

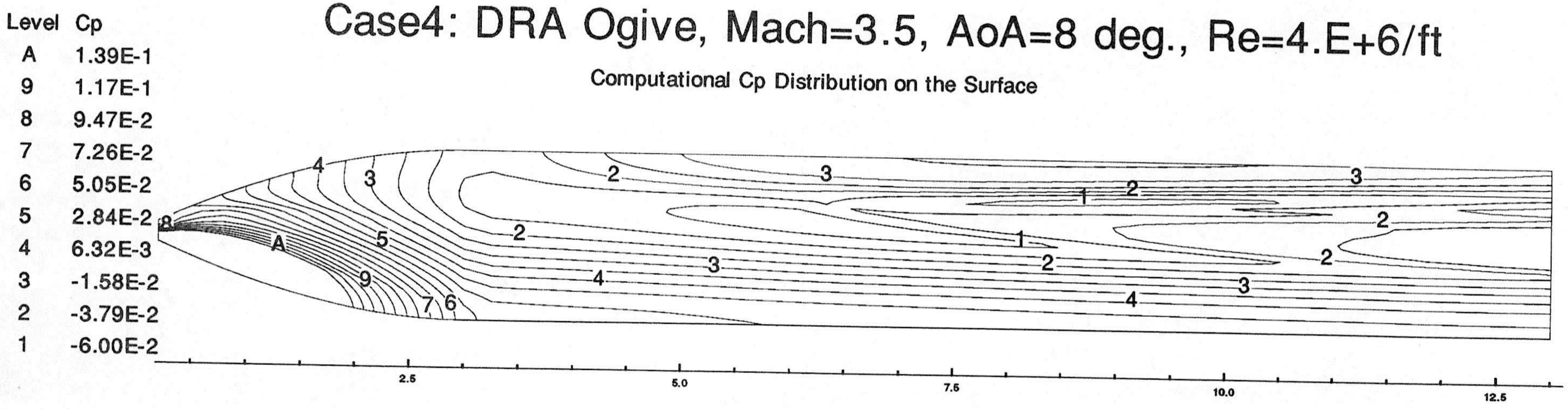

Fig. 11

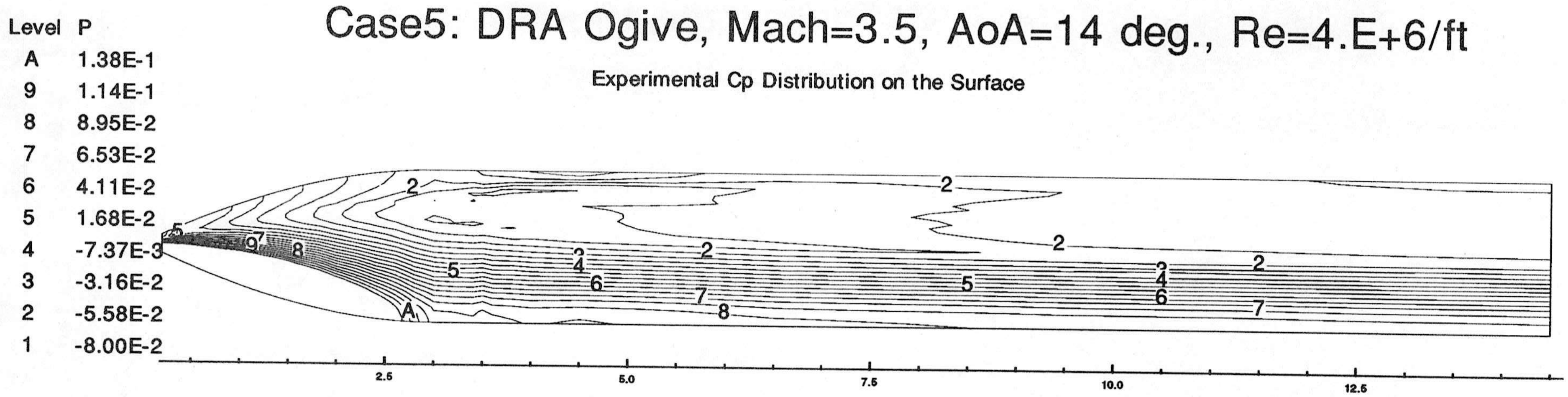
Case5: DRA Ogive, Mach=3.5, AoA=14 deg., Re=4.E+6/ft

Experimental Cp Distribution on the Surface

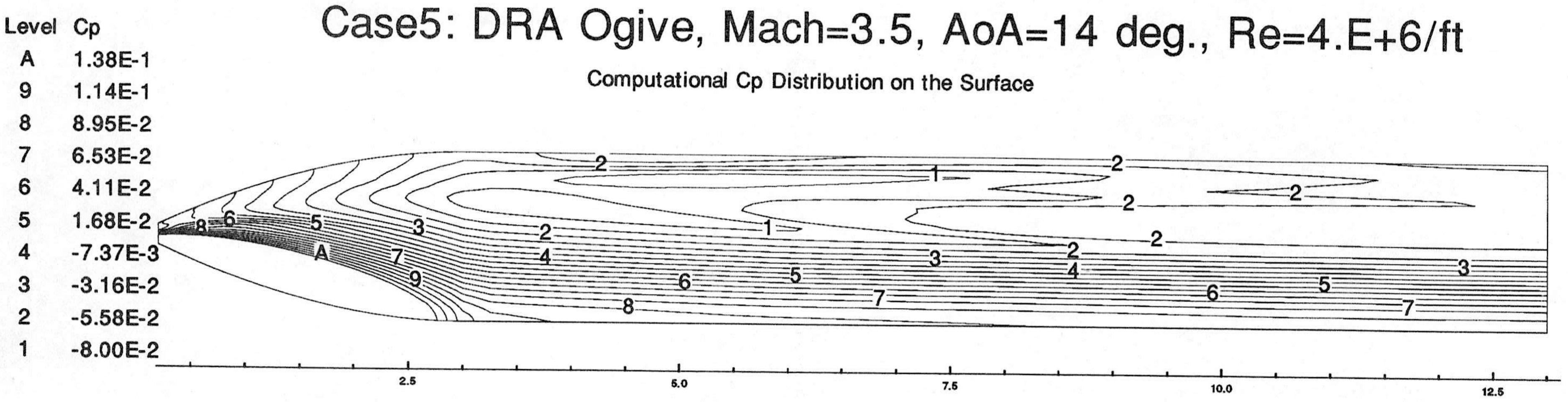
Case5: DRA Ogive, Mach=3.5, AoA=14 deg., Re=4.E+6/ft

Computational Cp Distribution on the Surface

Fig. 12

Case3: DRA Ogive, Mach=2.5, AoA=14 deg., Re=4.E+6/ft
Computational Stress Distribution on the Surface

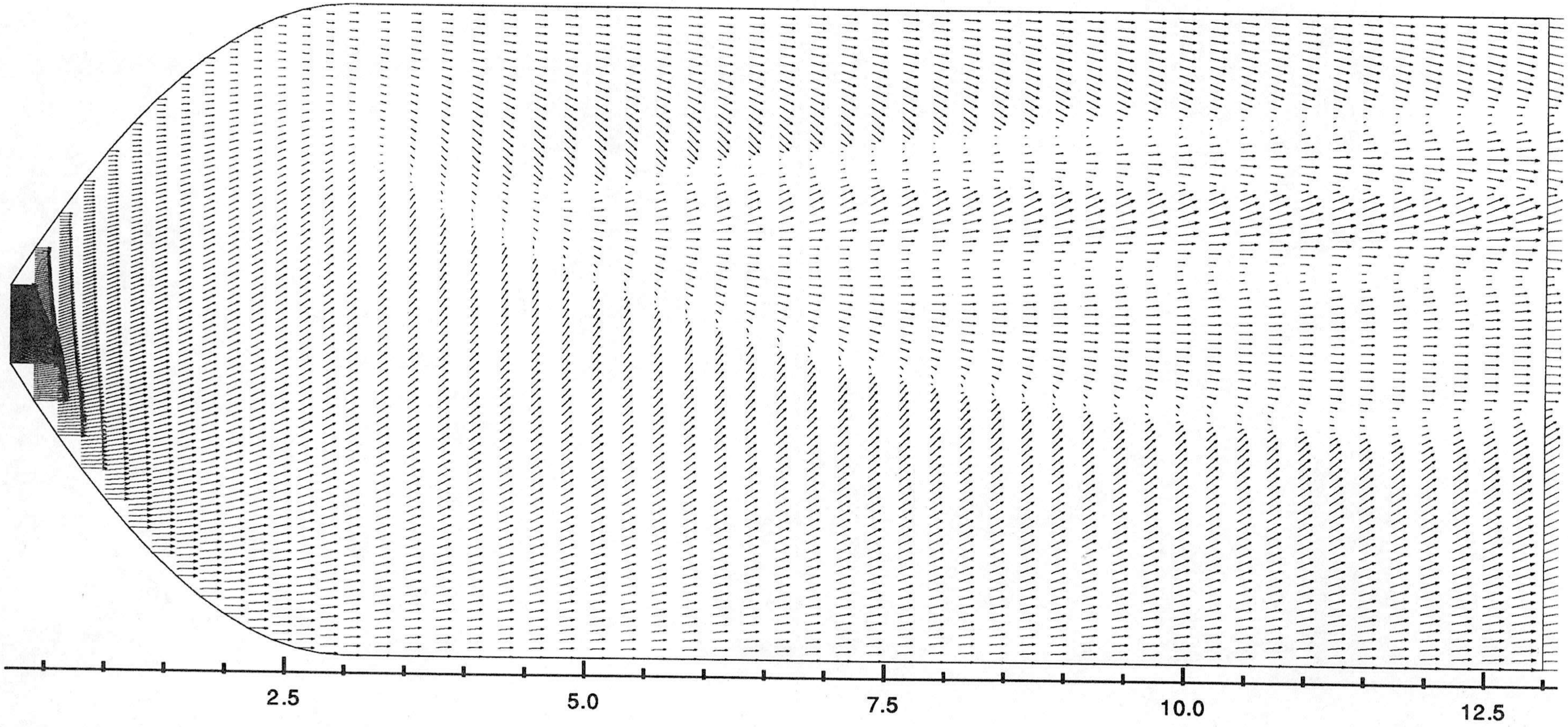

Fig. 13

Case3: DRA Ogive, Mach=2.5, AoA=14 deg., Re=4.E+6/ft
Computational Limit Stream Lines Distribution on the Surface

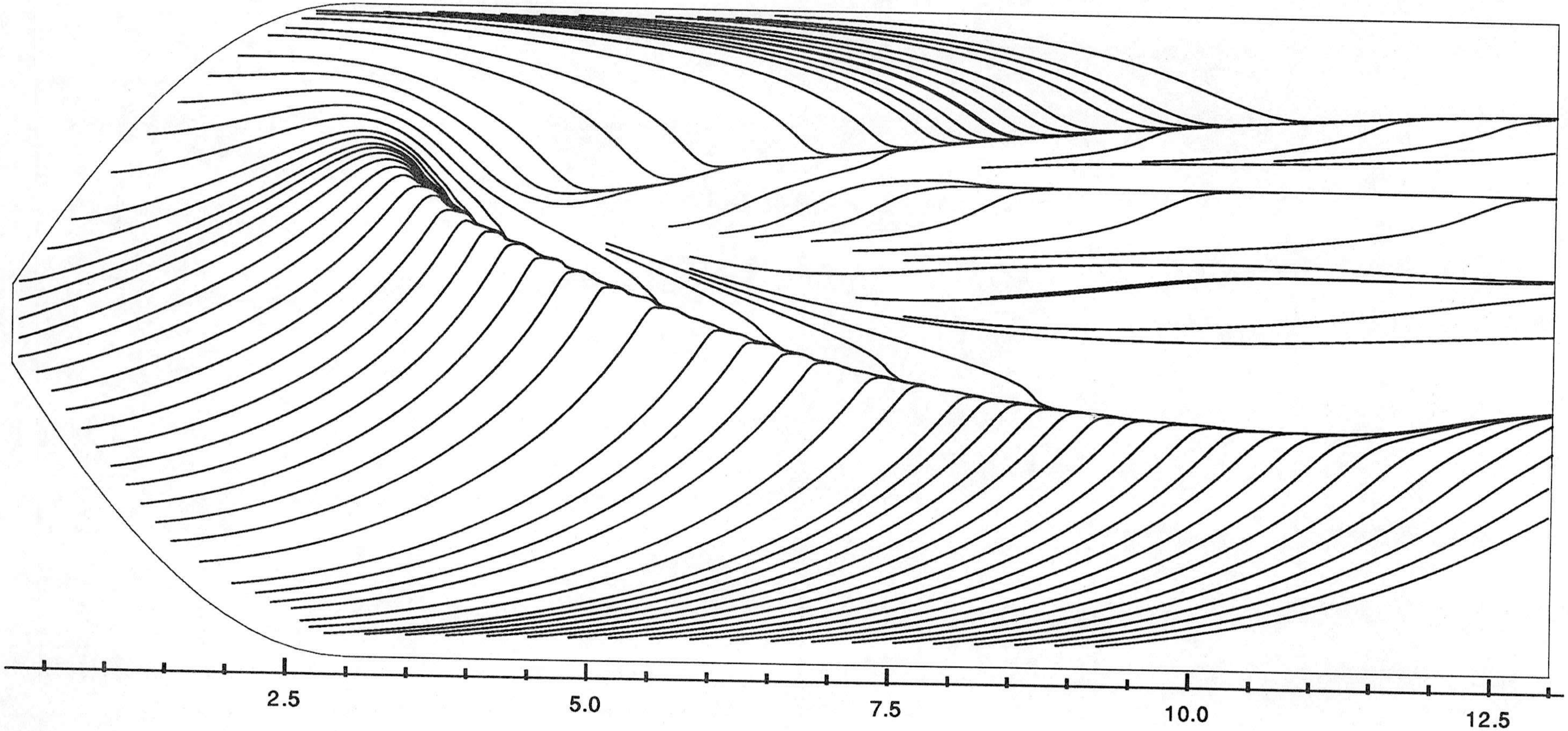

Fig. 14

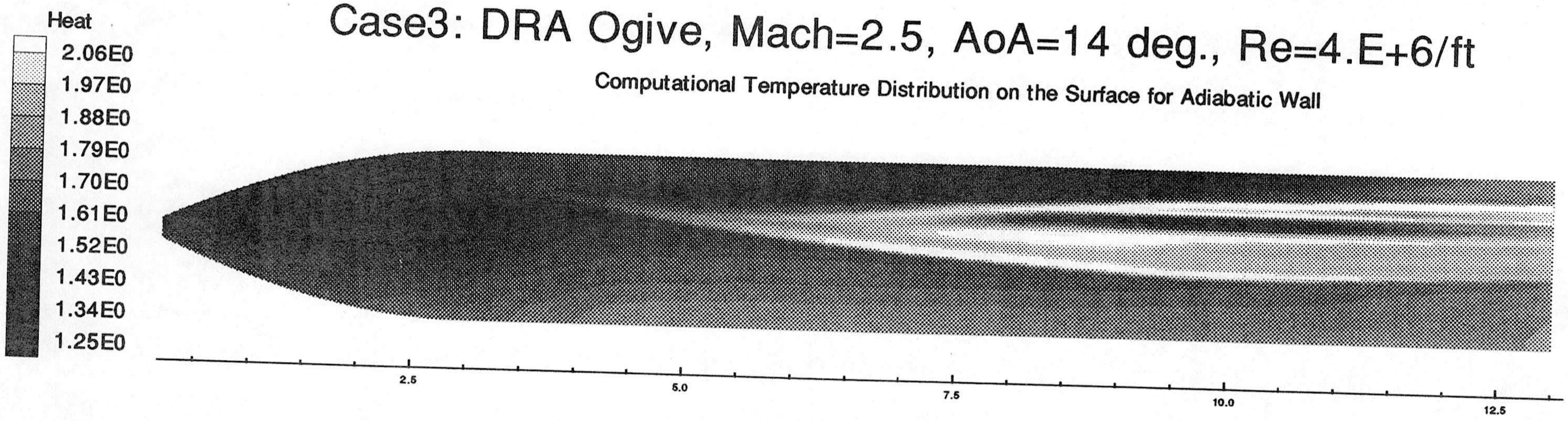
Case3: DRA Ogive, Mach=2.5, AoA=14 deg., Re=4.E+6/ft

Computational Temperature Distribution on the Surface for Adiabatic Wall

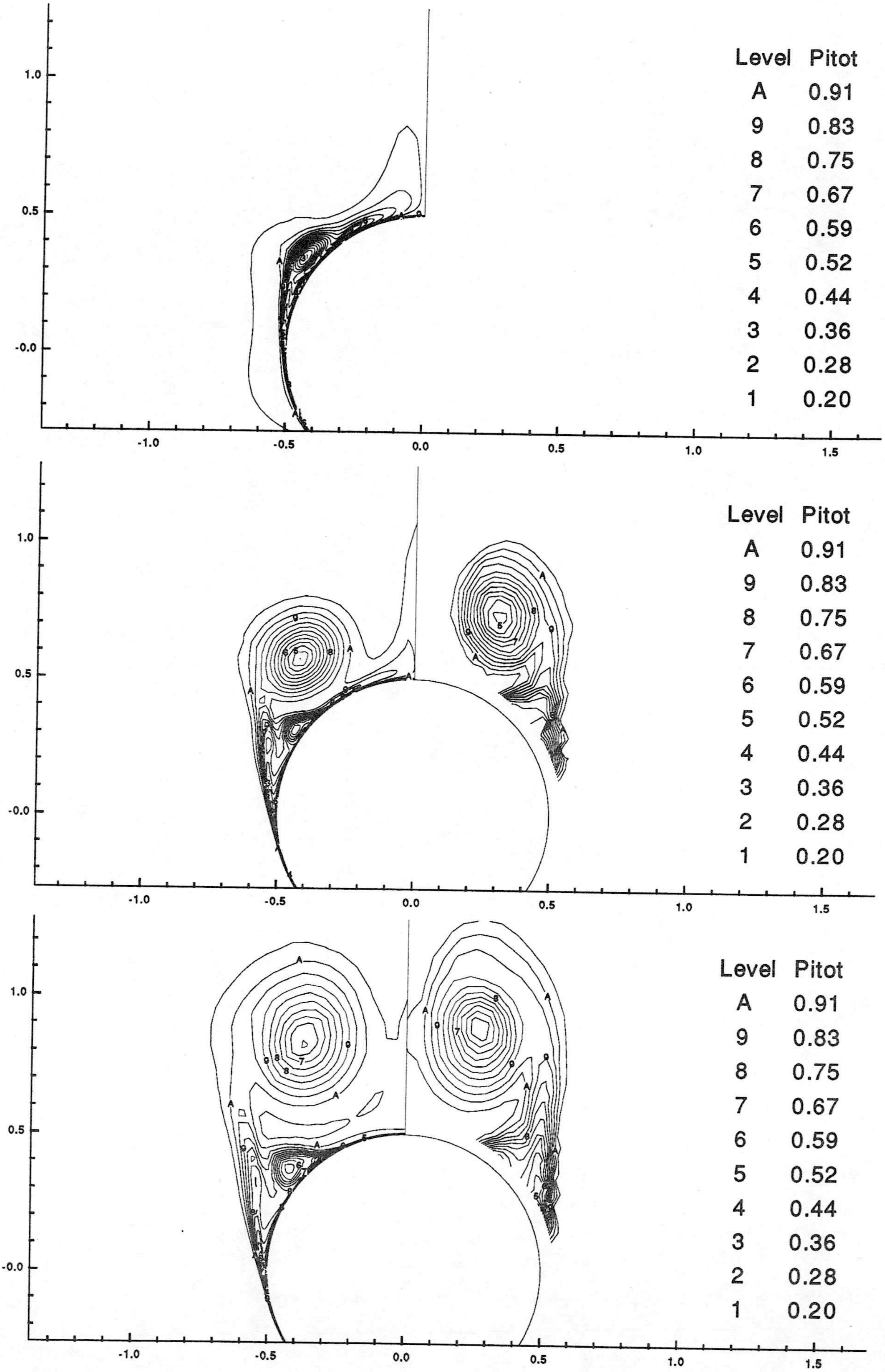
Level Pitot
A 0.91
9 0.83
8 0.75
7 0.67
6 0.59
5 0.52
4 0.44
3 0.36
2 0.28
1 0.20
1.0
0.5
-0.0
-1.0
-0.5
0.0
0.5
1.0
1.5
Level Pitot
A 0.91
9 0.83
8 0.75
7 0.67
6 0.59
5 0.52
4 0.44
3 0.36
2 0.28
1 0.20
1.0
0.5
-0.0
-1.0
-0.5
0.0
0.5
1.0
1.5
Level Pitot
A 0.91
9 0.83
8 0.75
7 0.67
6 0.59
5 0.52
4 0.44
3 0.36
2 0.28
1 0.20
1.0
0.5
-0.0
-1.0
-0.5
0.0
0.5
1.0
1.5

Fig. 15

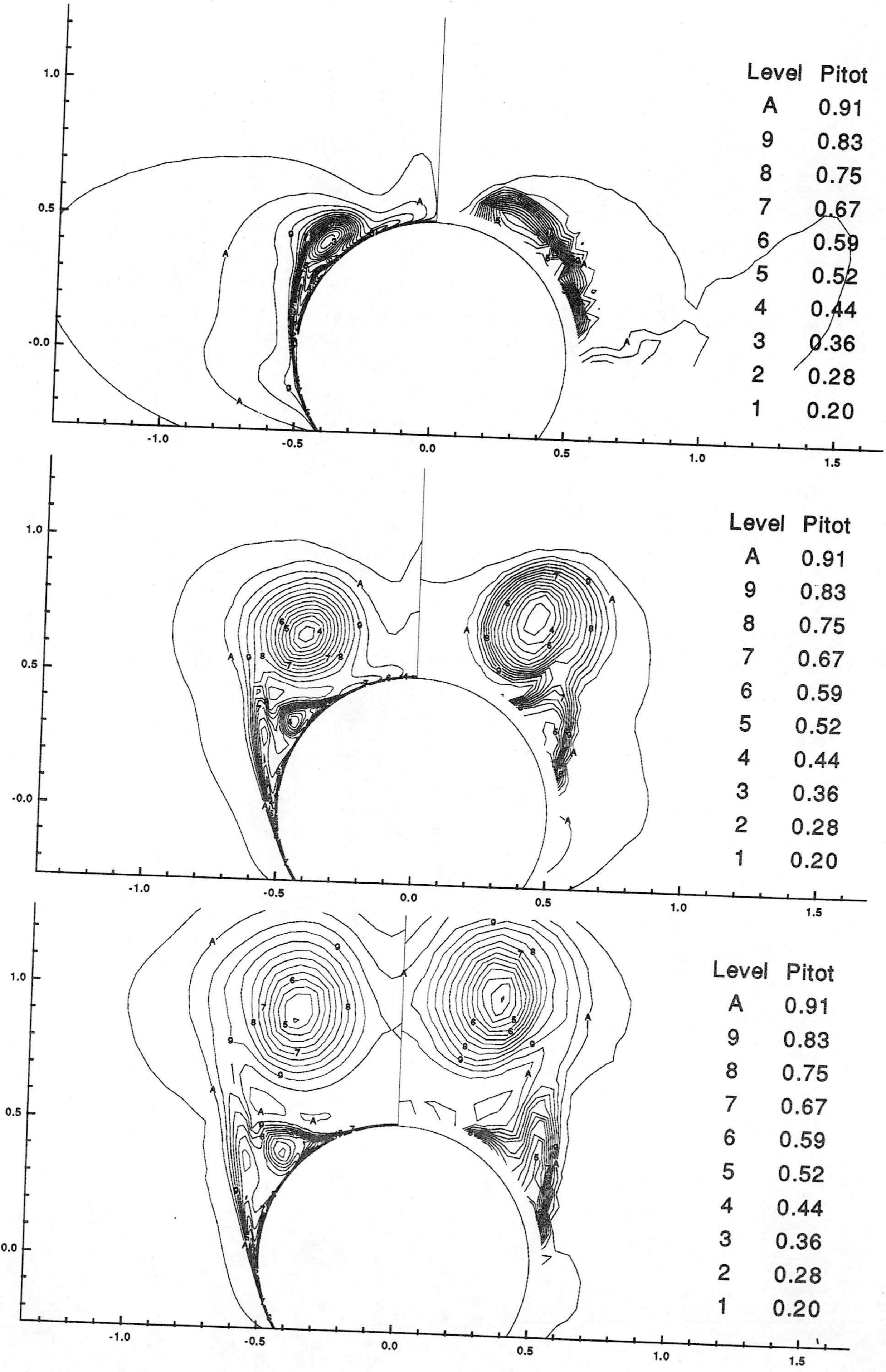
Level Pitot
A 0.91
9 0.83
8 0.75
7 0.67
6 0.59
5 0.52
4 0.44
3 0.36
2 0.28
1 0.20
1.0
0.5
-0.0
-1.0
-0.5
0.0
0.5
1.0
1.5

Fig. 16

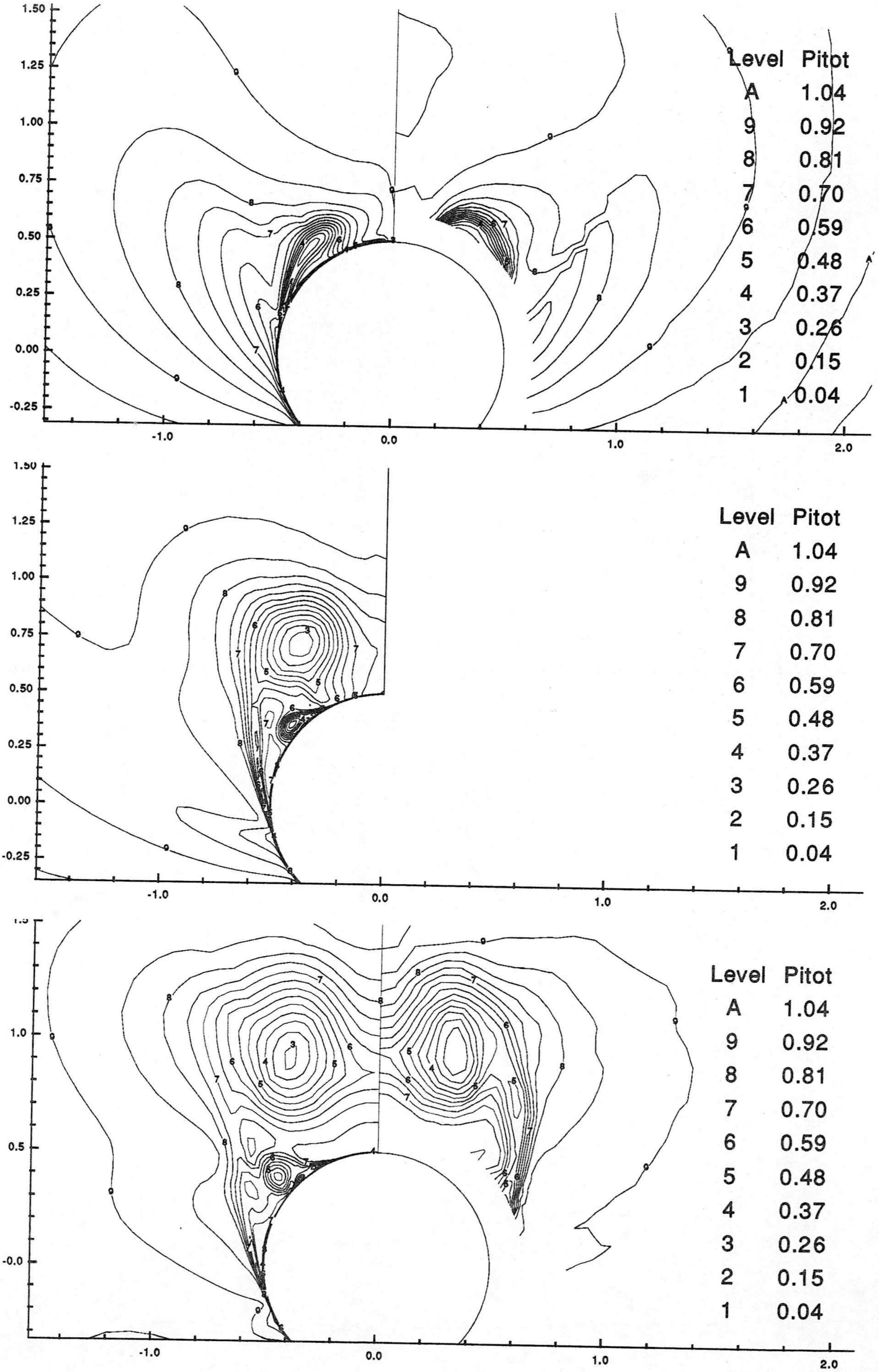
1.50
1.25
1.00
0.75
0.50
0.25
0.00
-0.25
-1.0
0.0
1.0
2.0
Level Pitot
A 1.04
9 0.92
8 0.81
7 0.70
6 0.59
5 0.48
4 0.37
3 0.26
2 0.15
1 0.04
1.5
1.0
0.5
-0.0

Fig. 17

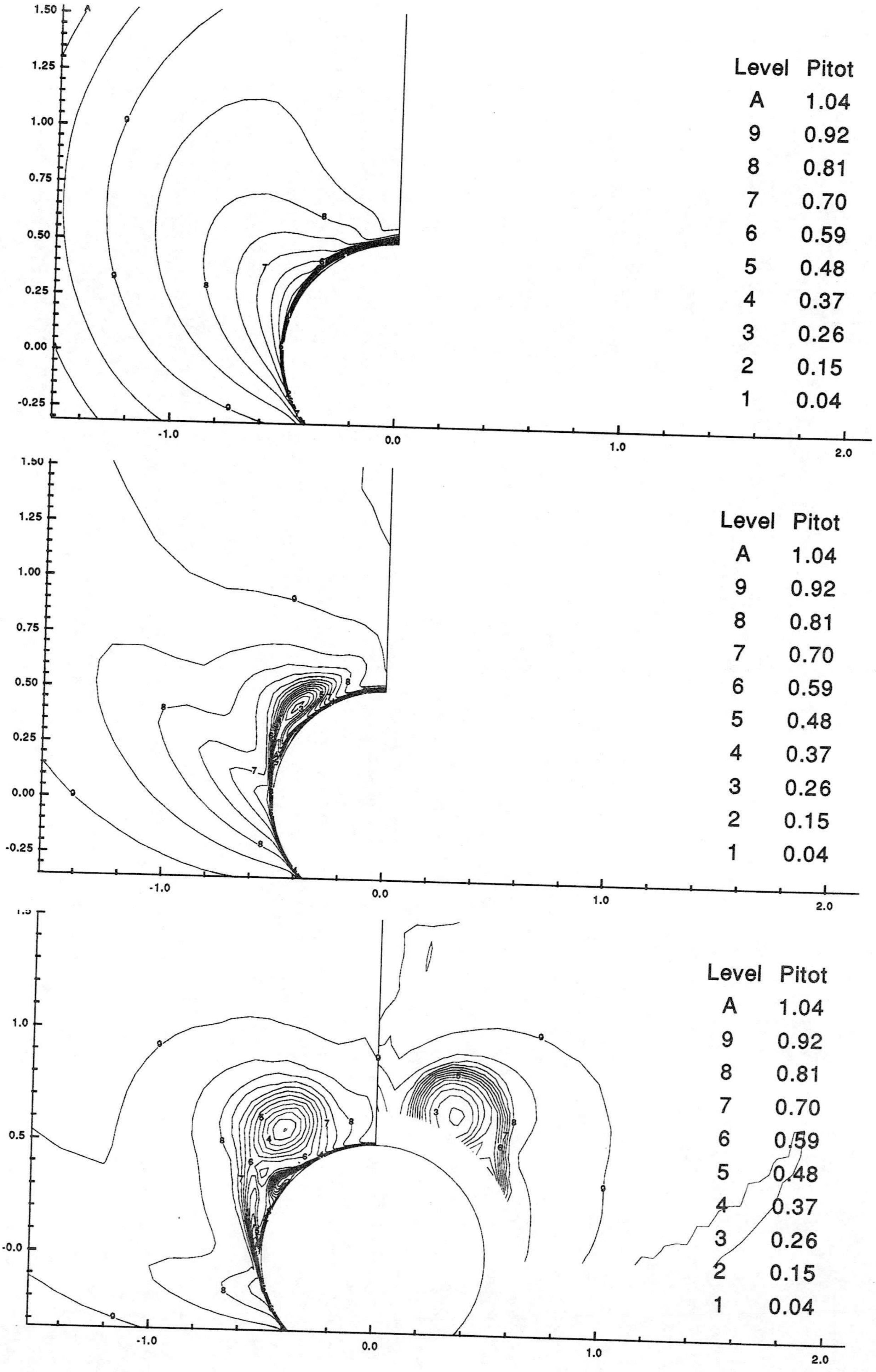
1.50
1.25
1.00
0.75
0.50
0.25
0.00
-0.25
-1.0
0.0
1.0
2.0
A
9
8
7
Level Pitot
A 1.04
9 0.92
8 0.81
7 0.70
6 0.59
5 0.48
4 0.37
3 0.26
2 0.15
1 0.04
1.50
1.25
1.00
0.75
0.50
0.25
0.00
-0.25
-1.0
0.0
1.0
2.0
9
8
7
4
3
Level Pitot
A 1.04
9 0.92
8 0.81
7 0.70
6 0.59
5 0.48
4 0.37
3 0.26
2 0.15
1 0.04
1.5
1.0
0.5
-0.0
-1.0
0.0
1.0
2.0
9
8
7
6
5
4
3
Level Pitot
A 1.04
9 0.92
8 0.81
7 0.70
6 0.59
5 0.48
4 0.37
3 0.26
2 0.15
1 0.04

Fig 18.

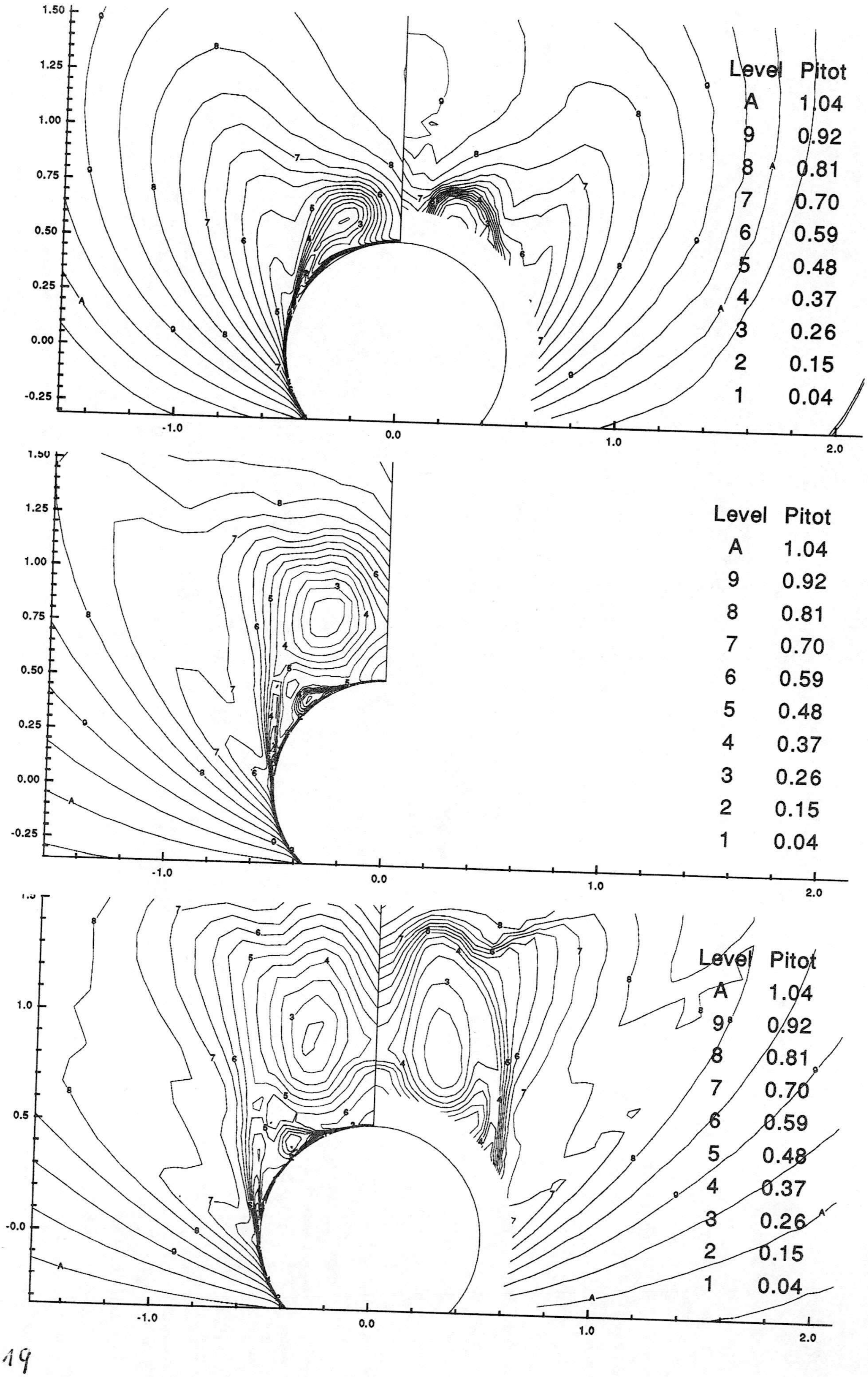
1.50
1.25
1.00
0.75
0.50
0.25
0.00
-0.25
-1.0
0.0
1.0
2.0
Level Pitot
A 1.04
9 0.92
8 0.81
7 0.70
6 0.59
5 0.48
4 0.37
3 0.26
2 0.15
1 0.04
1.50
1.25
1.00
0.75
0.50
0.25
0.00
-0.25
-1.0
0.0
1.0
2.0
Level Pitot
A 1.04
9 0.92
8 0.81
7 0.70
6 0.59
5 0.48
4 0.37
3 0.26
2 0.15
1 0.04
1.5
1.0
0.5
-0.0
-1.0
0.0
1.0
2.0
Level Pitot
A 1.04
9 0.92
8 0.81
7 0.70
6 0.59
5 0.48
4 0.37
3 0.26
2 0.15
1 0.04

Fig. 19

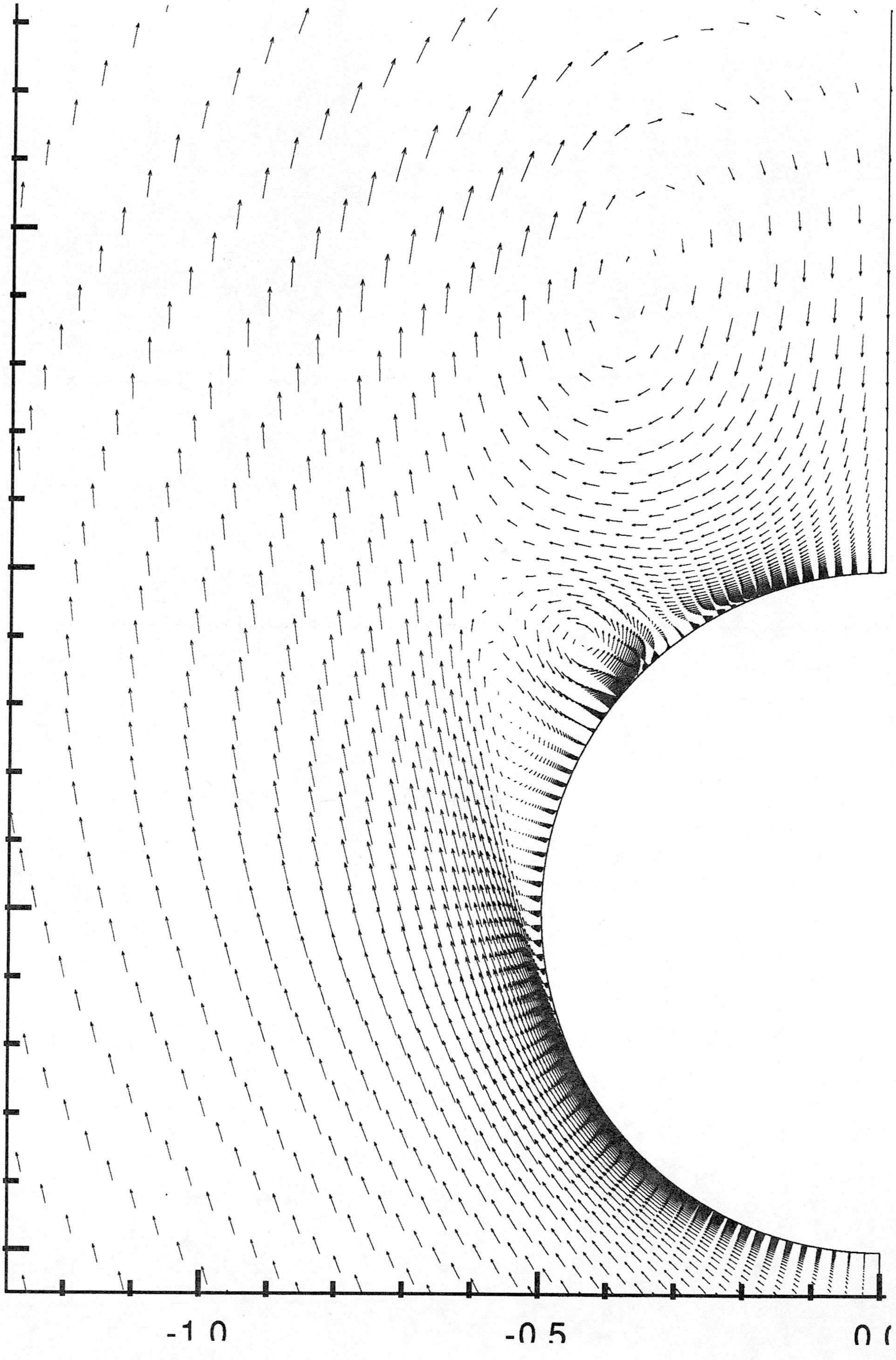

Fig. 20

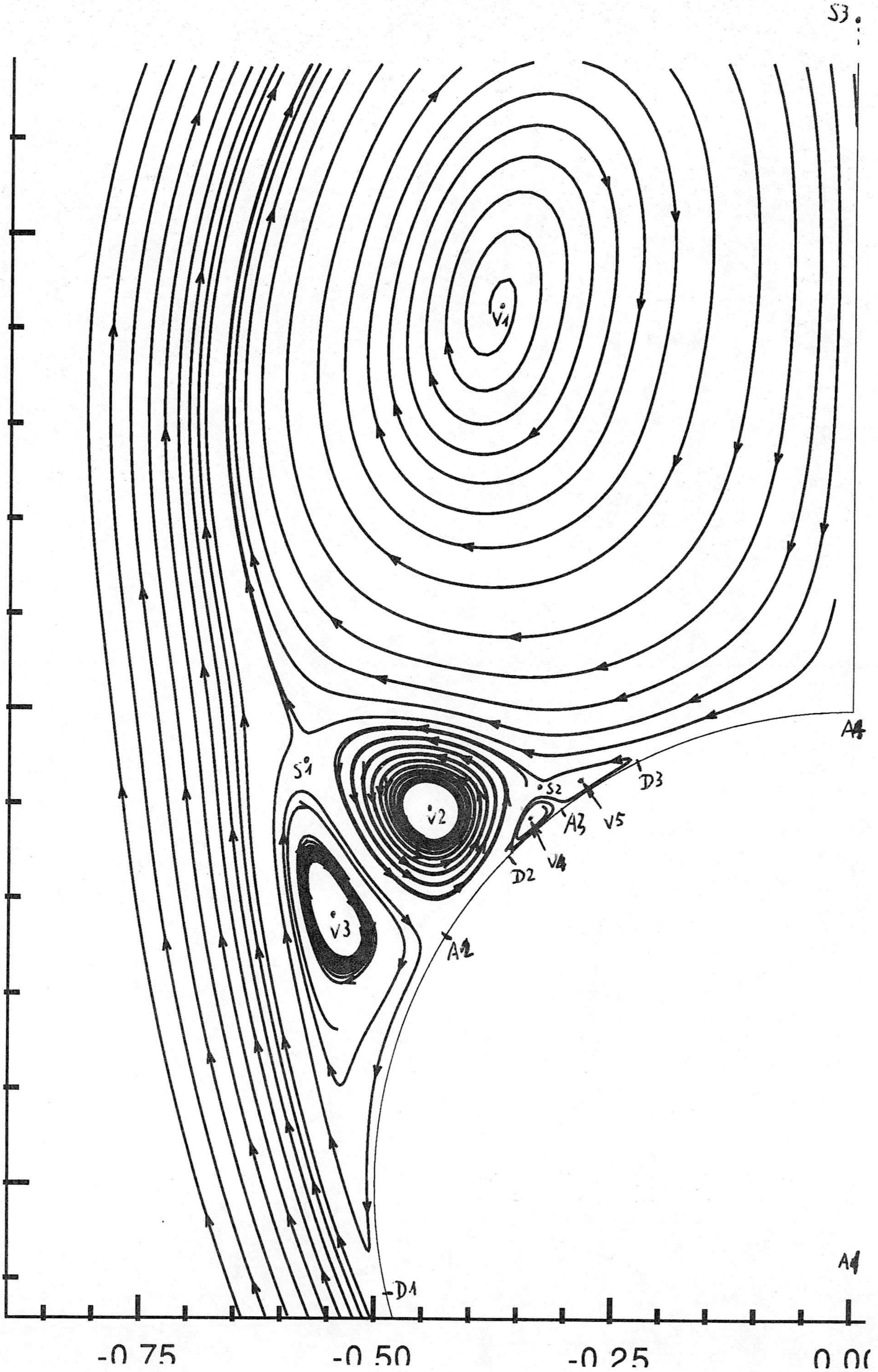

Fig. 21

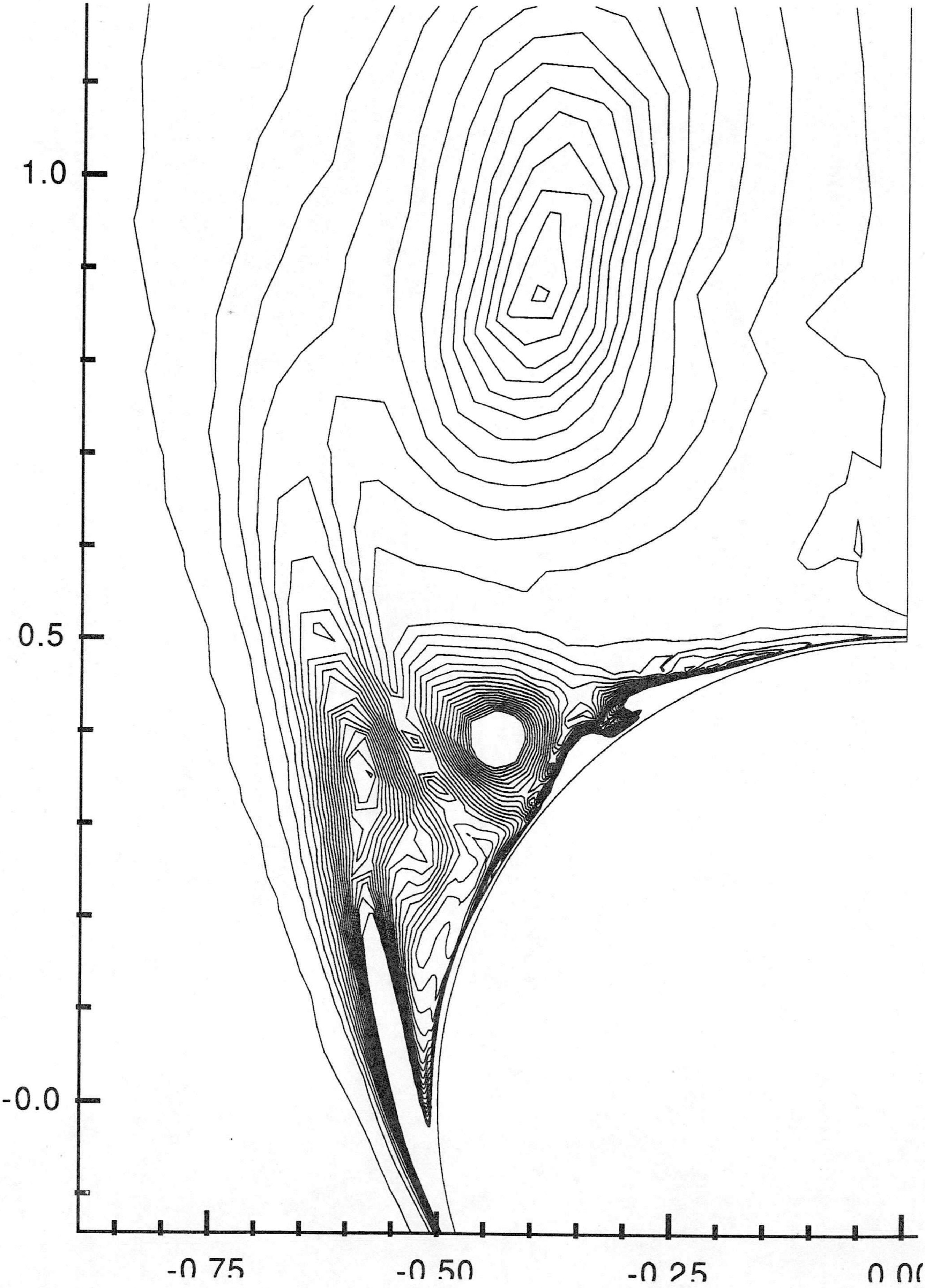

Fig. 22.

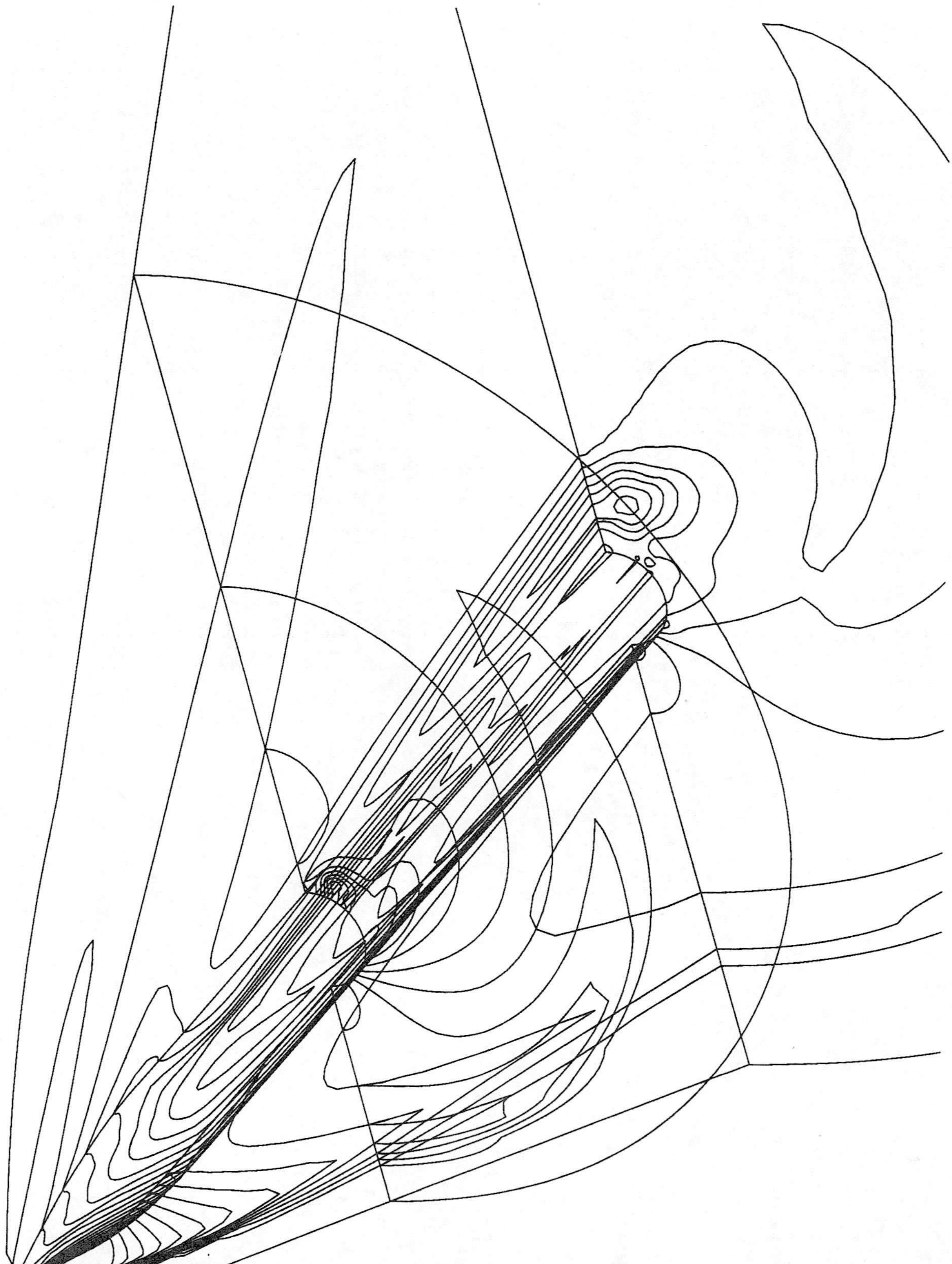

Fig. 23.